Czech Technical University in Prague
Faculty of Nuclear Sciences and Physical Engineering
Department of Physics

Programme: Applied natural sciences
Branch of Study: Physics and Technology of Nuclear Fusion

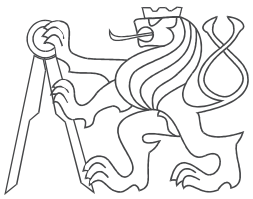

Handling and Transport of Laser-Driven Ion Beams

Manipulace a transport iontových paprsků řízených laserem

BACHELOR'S DEGREE PROJECT

Author: Martina Žáková
Supervisor: Daniele Margarone, PhD.
Consultant: Mario Maggiore, PhD.
Submitted in: July 2013

VLOZENI ZADANI PRACE S PODPISEM DEKANA

Prohlášení

Prohlašuji, že jsem svou bakalářskou práci vypracovala samostatně a použila jsem pouze podklady uvedené v přiloženém seznamu.

V Praze dne ....

Martina Žáková

Acknowledgements

I would like to thank my supervisor Daniele Margarone, PhD. and consultant Mario Maggiore, PhD. for providing expert advices, kind comments, willingness and friendly approach during this work.

Název práce:

Manipulace a transport iontových paprsků řízených laserem

Autor: Martina Žáková

Obor: Fyzikální inženýrství

Druh práce: Bakalářská práce

Vedoucí práce: Daniele Margarone, PhD.
ELI-Beamlines Project; Fyzikální ústav Akademie věd ČR

Konzultant: Mario Maggiore, PhD.
ELI-Beamlines Project; Fyzikální ústav Akademie věd ČR

Abstrakt:

První část práce popisuje hlavní teoretické myšlenky dějů obsažených v procesu urychlování iontových svazků laserem, jako je například laserová absorpce či nejběžnější urychlovací mechanismy (jmenovitě TNSA nebo RPA režimy). Následně práce pokračuje výkladem chování nabitého částicového svazku v magnetickém poli solenoidu. Rovněž se soustřeďuje na dynamický popis svazku v solenoidu a interpretuje teorii svazkové emitance. Obsažen je také popis transformace z kartézských do cylindrických souřadnic. Hlavním přínosem práce je vytvoření programu (v MATLABu), který nalézá souřadnice bodů trajektorie nabité částice (nebo celého částicového svazku) v magnetickém poli solenoidu a současně uvažuje emitanci svazku. Program přispívá k části Zachycení & Selekce v plánovaném zařízení ELIMED beamline, které bude v provozu v rámci projektu ELI-Beamlines. ELIMED se bude soustředit na budoucí aplikace, například laserem řízenou hadronovou terapii, která je diskutována na závěr práce, a to jak s fyzikálním, tak s medicínským odůvodněním.

Klíčová slova: urychlování iontů laserem, magnetické pole v solenoidu, emitance, transport iontových svazků, hadronová terapie

Title:

Handling and Transport of Laser-Driven Ion Beams

Author: Martina Žáková

Abstract:

The first part of the work describes the basic theoretical concepts of processes involved in laser driven ion acceleration, such as laser absorption and the most common acceleration mechanisms (namely TNSA and RPA regimes). The thesis continues with describing the behaviour of charged particle beams in a solenoid magnetic field. It also focuses on beam dynamics in a solenoid and interprets theory about beam emittance. Moreover, the needed information about transformation from a Cartesian coordinate system to a cylindrical one is included. The main part of this work is the development of a matlab program which can compute the trajectory coordinates of a charged particle (or the whole particle beam) in a solenoid magnetic field taking into account the beam emittance. In fact, the program contributes to the Capturing & Selection section in the layout of the ELIMED beamline, which will be operational at ELI-Beamlines. ELIMED will focus on future application, e.g. laser driven hadrontherapy as dicussed in the final part of the thesis with both clinical and physical rationale.

Key words: laser driven ion acceleration, solenoid magnetic field, emittance, ion beam transport, hadrontherapy

Contents

Introduction

The plasma state is considered as the fourth state of matter and his abundance in the universe (mainly because of stars) makes extremely important the production of plasmas in laboratory. Among various technique to produce this state of matter in laboratory, laser plasma physics is a field of big interest because of its implications in basic science, thermonuclear fusion, astrophysics, material science, particle acceleration, medicine, etc. Several tens of MeV ions can be accelerated from a plasma produced by a high intensity, short laser pulse. Very strong electric fields can be sustained in plasma, thus generating large charge displacement and, in turn, acceleration gradients in very short distances (typically few tens of micrometers). Many application of laser driven ion beams are foreseen, e.g. triggering and control of nuclear reactions, production and probing of warm dense matter, fast ignition of fusion targets, etc. Medical laser-driven hadrontherapy is one of the most attractive application, in fact, the great advantage of protons/ions is associated with the delivering of the most of their energy at the end of their path during the propagation in tissues, differently from electron and X-rays. This characteristic, known as energy release in the Bragg peak, allows to treat only the tumor cells and not to damage the healthy surrounding tissue. Although several hadrontherapy facilities based on conventional accelerators are operational worldwide, laser-driven hadrontherapy centers are still not widely present due to the high costs associated with a standard with standard accelerators, complex beam transport and shielding systems, large gantries. A future hadrontherapy center based on laser driven acceleration could be very compact and cost-effective. Neverteless, currently such a system does not fit with the strict radiological requirements (ion energy, ion dose, etc.). Moreover, beside technical aspects, the biological consequences of short ion bunches associated with ultrashort laser pulses have to be better understood.
One of the current limitation of laser driven ion sources is the characteristic large divergence of such beams. Thus, this is one of the issue to be solved. The goal of this thesis work is to propose a simple method for reducing the divergence of a proton beam accelerated by lasers through the use of magnetic solenoids.
The first part of the thesis deals with basic concepts of high intensity laser matter interaction and ion acceleration mechanisms, as well as charged particle motion in solenoid magnetic fields and definition of typical particle beam parameters. The original contribution is shown in the third chapter through the description and the results of a developed matlab program calculating trajectories of laser accelerated ions in a solenoid field. Potential applications are discussed in the final part of the work.

Various literature sources have been used in the thesis. Online available sources (websites, wikipedia, etc.) have been useful for having an overview of the wide field of interest for this thesis. Then, scientific articles (mostly not open source) have been essential for a deeper understanding of specific topics reported in the thesis. Also books have been used (mainly

"High power laser-matter interaction" by P. Mulser and D. Bauer, and "Essential MATLAB for engineers and scientists" by B. Hahn and D. Valentine, etc). The first book was primarily used for drafting the first chapter. The second book was used for familiarizing with the programming syntax in MATLAB. Finally websites of prestigious hospitals, research medicinal centers and appropriate articles about the specific topic served for drafting the last chapter on potential use of laser driven proton beams for treatment of tumours (e.g. hadrontherapy).

In fact the potential future applications of laser driven ion beams in medicine is the main reason which motivated me in choosing this topic for my bachelor thesis. Furthermore, the possibility to give my personal contribution to "Handling and Transport of Laser-Driven Ion Beams" by theoretical calculation was very interesting to me, especially because it allowed me to work in the framework of the future ELI-Beamlines facility in the Czech Republic, through the optimization of the ELIMED beamline design.

Chapter 1

Laser driven proton acceleration

The year 2000 was crucial in making the laser driven ion acceleration attractive for applications. Ions having energies up to a few MeVs had been observed in high-intensity laser matter interaction experiments considering different targets. Nevertheless, in 2000 an intense emission of multi-MeV protons from a several microns thick targets (solid, metallic or plastic) was detected in three independent experiments. Those experiments are described in:

- Maksimchuk et al., 2000 – $I_L = 3{\cdot}10^{18}$ W cm^{-2}, $N_p \gtrsim 10^9$ and $E_p = 1,5$ MeV,
- Clark et al., 2000 – $I_L = 5{\cdot}10^{19}$ W cm^{-2} $N_p \sim 10^{12}$ and $E_p = 18$ MeV,
- Snavely et al., 2000 – $I_L = 3{\cdot}10^{20}$ W cm^{-2} $N_p \sim 2 \cdot 10^{13}$ and $E_p = 58$ MeV,

where I_L, N_p and E_p are – laser intensities, number of protons and maximum ion energy observed. The simple set-up of these experiments can be seen in Fig. 1.1.

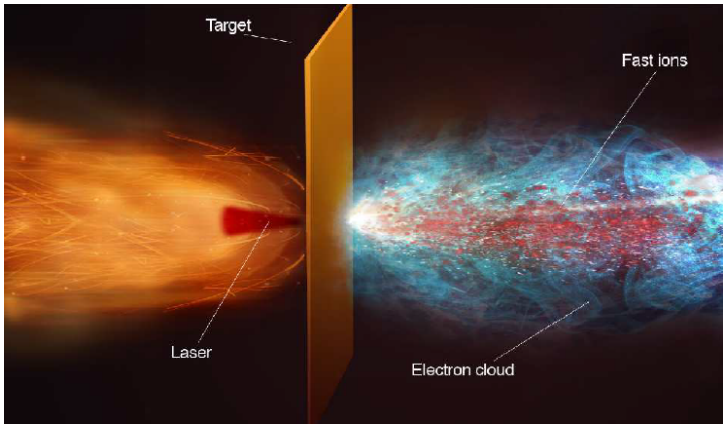

Figure 1.1: An artistic view of a typical experiment on proton emission from laser-irradiated solid targets; [14]

After this period laser driven proton acceleration became more and more interesting for future applications – laser triggering, nuclear reactions control, production and probing of warm dense matter, "fast ignition" of Inertial Confinement Fusion targets, cancer treatment etc. Contrast to electrons and X-rays, protons and light ions deliver the most of their energy at the end of their path (Bragg peak). This is very convenient for applications in hadrontherapy

because the particles can pass through healthy tissue without damaging it.
Currently, the mechanisms of laser driven acceleration are being improved to obtain higher energies per nucleon up to hundreds MeV. New generation of lasers will allow to achieving much higher intensities than the present ones, thus having the way towards future applications.

1.0.1 Laser beam interaction with matter

A laser pulse can be described by an electromagnetic wave packet which is a solution of Maxwell's equations [12]:

$$\nabla \times \vec{E} = -\frac{1}{c}\frac{\partial}{\partial t}\vec{B}, \qquad \nabla \cdot \vec{B} = 0, \tag{1.1}$$

$$\nabla \times \vec{B} = \frac{4\pi}{c}\vec{j} + \frac{1}{c}\frac{\partial}{\partial t}\vec{E}, \qquad \nabla \cdot \vec{E} = 4\pi\rho, \tag{1.2}$$

where $\vec{E}$ is electric field, $\vec{B}$ is magnetic field, $\vec{j}$ is current density, ρ is charge density, c is speed of light and t is time. In vacuum $\rho = 0$ and $\vec{j} = 0$ are valid, because there are no charges and no currents. This situation will be changed when the laser pulse propagates in material medium which creates plasma – in this case the sources of both will appear.
Scalar and vector potential Φ, $\vec{A}$ are bounded with electric and magnetic field by following equations:

$$\vec{B} = \nabla \times \vec{A}, \qquad \vec{E} = -\nabla\Phi - \frac{1}{c}\frac{\partial}{\partial t}\vec{A}. \tag{1.3}$$

If we consider $\nabla \cdot \vec{A} + \frac{1}{c}\frac{\partial}{\partial t}\Phi = 0$ and rotation identity $\nabla \times \nabla \times \vec{A} = \nabla(\nabla \cdot \vec{A}) - \Delta\vec{A}$ we can rewrite Maxwell's equations in this way:

$$\nabla \times \vec{B} = \frac{4\pi}{c}\vec{j} + \frac{1}{c}\frac{\partial}{\partial t}\vec{E} \qquad \rightarrow \qquad \Delta\vec{A} - \frac{1}{c^2}\frac{\partial^2}{\partial t^2}\vec{A} = -\frac{4\pi}{c}\vec{j}. \tag{1.4}$$

Another wave equation we can derive very similarly from the microscopic Gauss's law:

$$\nabla \cdot \vec{E} = 4\pi\rho \qquad \rightarrow \qquad \Delta\Phi - \frac{1}{c^2}\frac{\partial^2}{\partial t^2}\Phi = -4\pi\rho. \tag{1.5}$$

As we have already discussed for vacuum, the relations $\rho = 0$ and $\Phi = 0$ are valid, that makes the condition $\nabla \times \vec{A} = -\frac{1}{c}\frac{\partial}{\partial t}\Phi$ zero and we get a following relation for electric field: $\vec{E} = -\frac{1}{c}\frac{\partial \vec{A}}{\partial t}$.

Now, take a look at the case of two dimensional waves in x-z plane. Then $A_x = \frac{\partial \vec{A}}{\partial z}$ and $A_z = \frac{\partial \vec{A}}{\partial x}$, where $A = A(x, z)$. Finally we check the condition $\nabla \cdot \vec{A} = 0$ by a simple substitution into the formula – $\nabla \cdot \vec{A} = \frac{\partial A_x}{\partial x} + \frac{\partial A_y}{\partial y} + \frac{\partial A_z}{\partial z} = 0$. Using relation (1.3) and conditions which we get, the electric field is given by free components:

$$E_x = -\frac{1}{c}\frac{\partial}{\partial t}\frac{\partial}{\partial z}A, \qquad E_y = 0, \qquad E_z = \frac{1}{c}\frac{\partial}{\partial t}\frac{\partial}{\partial t}A. \tag{1.6}$$

Magnetic field can also be divided into three components, which are given by the relations:

$$B_x = 0, \qquad B_y = \left(\frac{\partial^2}{\partial x^2} + \frac{\partial^2}{\partial z^2}\right)A, \qquad B_z = 0. \tag{1.7}$$

If the wave has its intensity high enough, then it interacts with medium (target) and changes properties of the particles which can move according to the equations of motion. Basically, it is just a form of the Lorentz equation:

$$\vec{F} = m\ddot{\vec{a}} = \frac{d\vec{p}}{dt}, \qquad \vec{F} = e(\vec{E} + \vec{v} \times \vec{B}) = e\vec{E} + \frac{e}{mc\gamma}\vec{p} \times \vec{B}, \tag{1.8}$$

where γ is a relativistic factor and $\gamma = \sqrt{1 + \frac{p^2}{m^2c^2}}$.

The relations for total current density $\vec{j}(\vec{r}, t)$ and total charge density $\rho(\vec{r}, t)$ can be written with consideration of Liouville theorem, where $f(\vec{r}, \vec{p}, t)$ is phase space density. According to the mentioned theorem the volume in phace space stays constant:

$$\frac{\partial f}{\partial t} + \frac{\vec{p}}{m\gamma}\frac{\partial f}{\partial \vec{r}} + \left(e\vec{E} + \frac{e}{mc\gamma}\vec{p} \times \vec{B}\right)\frac{\partial f}{\partial \vec{p}} = 0, \tag{1.9}$$

then for total current and charge density the following equations are valid:

$$\rho(\vec{r}, t) = e\int f(\vec{r}, \vec{p}, t)\mathrm{d}\vec{p}, \qquad \vec{j}(\vec{r}, t) = e\int \frac{p}{m\gamma} f(\vec{r}, \vec{p}, t)\mathrm{d}\vec{p}. \tag{1.10}$$

Further details are in [12].

As a consequence of high intensity laser interaction with matter, plasma is produced. One of the most relevant plasma parameters is the electron density, which determines the plasma oscillation frequency ω_p. The equality between the electron and critical electron densities n_e, n_c is equivalent to the equality between the laser and plasma frequencies ω, ω_p. The equations for n_c and ω_p are [14]:

$$\omega = \omega_p \quad \Leftrightarrow \quad \frac{2\pi c}{\lambda} = \sqrt{\frac{4\pi n_e e^2}{m_e}} \quad \Rightarrow \quad n_e = \frac{m_e\omega^2}{4\pi e^2} = n_c. \tag{1.11}$$

According to the relation between electron and critical density of the plasma we can divide the environement in two regions with two different values of the refractive index. The refractive index n is bounded with densities or frequencies through this simple relation:

$$n = \sqrt{1 - \omega_p^2/\omega^2} = \sqrt{1 - n_e^2/n_c^2}. \tag{1.12}$$

If the case that $n_e > n_c$ is valid we are in an *overdense* region with imaginary values of n. This means that the laser pulse cannot propagate. On the other hand if $n_e < n_c$ or $n_e \simeq n_c$ is valid, the refractive index has real values and all the plasma interactions occurs there and we are in an *underdense* region.
The relativity case is not so simple, because the refractive index n is non-linear. From [14] we can write a relation for the relativistic refractive index:

$$n = \sqrt{1 + \langle\vec{a}^2\rangle}, \tag{1.13}$$

where $\vec{a}$ is ratio between electromagnetic energy and electron rest mass energy $\vec{a} = e\vec{A}/m_ec^2$. Brackets mean the average value over the oscillation period.

The process of plasma penetration by laser is quite complicated because of nonlinearity in the wave equation and changing of the plasma density profile as a result of radiation pressure. Luckily, this problem can be solved via ponderomotive force as it is discussed in [14]. We only give a simple definition of this here, because we will use this term later [14]: "*We refer to the ponderomotive force as the slowly-varying, effective force describing the cycleaveraged motion of the "oscillation centre" of a charged particle in an oscillating non-uniform field, over a time scale longer than the oscillation period.*" But in our description of ponderomotive force, the "fast" oscillating components are not included.

We can divide interactions between laser pulse and solid target into pure and non-pure ones depending on pre-plasma generation. In fact a laser pre-pulse (or pedestal) can generate pre-plasma before the arrival of the main pulse and no genuine laser-solid interaction will occur.

1.0.2 Hot (fast) electrons

The potential of an electron plasma wave must have certain amplitude to trap a significant amount of electrons passing through. If the potential is not strong enough, the electrons will follow straight orbits. If the amplitude becomes bigger, the first particles, with their own velocity similar to the wave phase velocity v_φ, will be caught. In the region where v_φ increases, hot electrons take their place in the acceleration mechanisms. In the region where v_φ decreases, the electrons are trapped again and they give their extra energy back to the wave.
The energy absorbed from a laser pulse is transported by hot (or sometimes called "fast") electrons, which are driven by the Lorentz force on the surface of the overdense plasma. These relativistic electrons have "ponderomotive" energy given by the relations [14], [18]:

$$\varepsilon_p = m_e c^2(\gamma - 1) = m_e c^2 \left(\sqrt{1 + \langle \vec{a}^2 \rangle} - 1\right) = m_e c^2 \left(\sqrt{1 + a_0^2/2} - 1\right), \tag{1.14}$$

$$a_0 = 0,85 \left(\frac{I[\text{W cm}^{-2}]\lambda^2[\mu \text{ m}]^2}{10^{18}}\right)^{1/2}, \tag{1.15}$$

a_0 is dimensionless amplitude related to the intensity I. The intesity is bounded with the electric field via the relation $I = c\langle E^2 \rangle / 4\pi$.
As we will discuss later in this chapter, hot electrons are crucial for acceleration of protons and heavy ions.

1.1 High intensity laser absorption mechanisms

Absorption mechanism can be most globaly described via the solution of Vlasov-Maxwell system which contains all the effects leading to absorption. Vlasov-Maxwell system of equations is a description of interactive system consisting of charged particles in plasma which create a self-consistent collective field. The equations corresponding to this problem are the Maxwell equations (1.1), (1.2) and relations for total current and charge density (1.10), where the function $f(\vec{r}, \vec{p}, t) = f_i(\vec{r}, \vec{p}, t) - f_e(\vec{r}, \vec{p}, t)$ is difference between distribution functions for plasma ions and electrons. Finally, the system of equations is finalized by Boltzmann Transport

Equations [42]:

$$\frac{\partial f_e}{\partial t} + \vec{v_e} \cdot \nabla f_e - e\left(\vec{E} + \frac{1}{c}(\vec{v} \times \vec{B})\right) \cdot \frac{\partial f_e}{\partial \vec{p}} = 0, \tag{1.16}$$

$$\frac{\partial f_i}{\partial t} + \vec{v_i} \cdot \nabla f_i - e\left(\vec{E} + \frac{1}{c}(\vec{v} \times \vec{B})\right) \cdot \frac{\partial f_i}{\partial \vec{p}} = 0. \tag{1.17}$$

There are many very interesting processes that are worth mentioning like anomalous skin effect, vacuum heating (electrons cross the plasma boundary and return back with high energy), Resonance absorption or Collisional absorption. Here we will describe only the last two mechanisms [13].

1.1.1 Resonance absorption (RA)

We assume collective behaviour of plasma, in the sense that long-range forces prevail over short-range forces. The process of plasma wave excitation over the critical layer is based on non-locally energy transfer in the plasma by the laser, when a P-polarized light has a component of the electric field in the laser direction. The critical layer is associated with the critical density.
In a constant plasma density profile (if we consider only resonance absorption without other interactions) the laser magnetic field does not undergo any change and the laser beam passes through without energy deposition. This means that constant plasma density profile in the underdense region can not lead to RA.
The resonance absorption mechanism can change for different plasma density profiles as described in [15]. It is necessary to change the computational approach of RA according to the plasma scale length L & laser wavelength ratio λ [15]:

- $\frac{L}{\lambda} \approx 0$ – resonance absorption does not exist here, the plasma density profile is a step function and the absorption in plasma is described by the Fresnel formulas.
- $\frac{L}{\lambda} \gg 1$ – the profile has a long slow varying form, we can use WKB approximation ("*WKB method is a method for finding approximate solutions for partial linear differential equations with spatially varying coefficients*" [43]). After that the absorption fraction is:

  $$f_{RA} \approx \varphi^2(\tau)/2, \tag{1.18}$$

  where $\varphi(\tau)$ is Ginzburg classical function which depends on the angle of incident θ. The maximum plasma electrostatic field is reached with $\theta = \frac{\pi}{4}$. Further details are reported in [15].
- $\frac{L}{\lambda} \ll 1$ – the profile is too sharp for using the WKB approximation, so we must solve this problem numerically [15].

1.1.2 Collisional absorption (CA)

Collisional absorption decreases when the laser intensity grows in contrast to Resonance absorption. This process is based on laser energy transfer to plasma electrons via columbian interactions (usually ion-electron collisions), that heat the plasma locally. CA causes energy

damping when the laser propagates through the plasma. The process can be characterized [15] by the absorption coefficient k_{abs}:

$$k_{abs} = \frac{\nu_{ei}}{c}\frac{n_e^2}{n_c}\sqrt{\left(1-\frac{n_e}{n_c}\right)^{-1}}, \tag{1.19}$$

where ν_{ei} is the collisional frequency between ions and electrons, index e means *electron* and c means *critical*.
Also in the case of CA the transported energy (via electromagnetic field) can be described according to $L-\lambda$ ratio [15]:

- $\frac{L}{\lambda} \approx 0$ – step function profile, Fresnel coefficients inform about the quantity of reflected/transmitted/absorbed light in the plasma medium
- $\frac{L}{\lambda} \gg 1$ – slowly varying plasma density profile, WKB approximation
- $\frac{L}{\lambda} \ll 1$ – steep plasma density profile, numerical simulations.

1.2 Rear and Front surface acceleration

We can divide ion acceleration mechanisms into two groups, according to in which side of the target the ions are accelerated from: *Rear surface acceleration* and *Front surface acceleration*. Now we give a brief overview of these two methods. Their basic structure can be seen in Fig. 1.2.

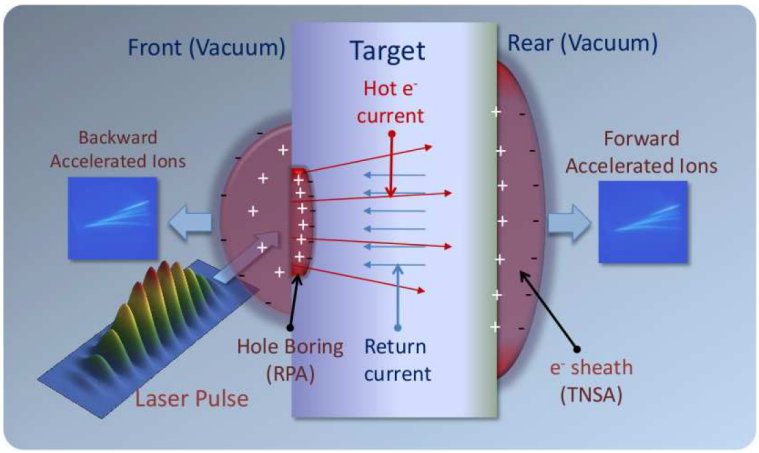

Figure 1.2: a simple sketch of laser-driven ion acceleration from thin foils; [14]

1.2.1 Rear Surface Acceleration

As we know from section 1.0.2 very intense current of hot electrons can be generated on the front side of the target. This current may or may not pass through the target. If the hot electrons reach the rear side of the target they cause an unbalance in charge. For better understanding, we can imagine this as a double layer of positive (ions) and negative (electrons) charges, which generates an electric field $\vec{E_s}$ (sheath electric field). We can write this vector field

as $\vec{E_s} = E_s \cdot \vec{n}$, where $\vec{n}$ is a vector perpendicular to the target surface. Since E_s must take back electrons with typical "temperature" T_h, we can describe the spatial extensity of the sheath L_s of the target via the relation:

$$eE_s \sim \frac{T_h}{L_s}, \tag{1.20}$$

where e is elementary charge and L_s can be approximated with the Debye length of the hot electrons. This approximation comes directly from the definition of Debye length that is the distance within which a significant charge separation can occur [34] – in other words the spatial extension of the sheath. Thus, we can write the formula for L_s as follows:

$$L_s \sim \lambda_{Dh} = \left(\frac{T_h}{4\pi e^2 n_h} \right)^2, \tag{1.21}$$

where n_h is density of the hot electrons. If we substitute typical values of T_h and n_h in (1.21), we obtain value for electric field E_s of about $10^{10} - 10^{-11}$ V $\cdot$ cm^{-1} [14]. This is an extremely high field which backholds an important number of escaping eletrons. Due to this field the atoms on the target rear side will be ionized and accelerated. The direction of the accelerated ions from the rear side is normal to the target (forward acceleration following the direction of the electric field). Typically energy of about $1-50$ MeV can be obtained from the following relation [14]:

$$\varepsilon_i \sim ZeE_sL_s \sim ZT_h. \tag{1.22}$$

If we consider (1.14) and assume $T_h \backsimeq \varepsilon_p$, the energy scales with $I^{\frac{1}{2}}$ (see (1.15)).
Since the target can contain hydrogen impurities on its surface, protons can be accelerated from this layer (target rear side in case of forward acceleration). In fact they are faster than other ions because of their higher charge-to-mass ratio. This is commonly known as TNSA mechanism which we will discuss in 1.3.

1.2.2 Front Surface Acceleration

There is also a possibility of developing a significant contribution to acceleration at the front surface of the target. The main idea is that the intense radiation pressure of the laser pulse pushes an overdense target inwards, which causes a sharp growth in density profile and changes the shape of its surface. This process is known as "hole boring".
The approximate relation for velocity v_{hb} of the plasma surface is obtained from balancing electromagnetic and mass momentum flows [14]:

$$I/c \sim n_i(m_i v_{hb})v_{hb}, \tag{1.23}$$

where n_i is the ion density. Then we can write the formula for the energy per nucleon:

$$\varepsilon_i = \frac{1}{2} m_p v_{hb}^2 \sim I/(An_i c). \tag{1.24}$$

In contrast with the rear surface acceleration we get energy scaling with laser intensity I instead of $I^{\frac{1}{2}}$, which is clearly a great advantage. The "hole boring" acceleration is considered as a particular regime of the radiation pressure acceleration (RPA), which will be discussed in chapter 1.4.

1.3 Target normal sheath acceleration (TNSA) regime

Target Normal Sheath Acceleration is a process (or a theoretical description) of accelerating ions from the rear side of the target. This acceleration is possible because of the interaction of an ultra intense short laser pulse irradiating a thin solid target. In addition, the acceleration is a consequence of strong charge separation generated by hot electrons expanding into vacuum and reaching the rear side of target. A part of the laser radiation is transformed into kinetic energy of relativistically hot ($T_h \approx$ few MeV) collisionless electrons, which can recirculate through the target and create a charge displacement. Thus a very intense electric field leads to ion acceleration and is caused by the relativistic electrons on the rear side. The field is mainly directed perpendicularly to target surface, so the ions are mainly accelerated in this direction. Moreover the ion beam can be relatively collimated.
Parameters of the intense electric field depend on the parameters of the electron distribution (temperature, divergence or amount of electrons) and on the parameters of the target surface (density shape).
As we have already said in chapter 1.2.1, the efficiency of TNSA depends on the mass in a way that ions with the largest charge-to-mass ratio are accelerated the most effectively. As already discussed due to hydrogen impurities on the target surface TNSA acceleration is commonly used for proton acceleration. Nevertheless, if impurities (H-ions) are removed before the interaction (e.g. by pre-heating the target) then several different sorts of ions may be accelerated via TNSA.
The experimental evidence of TNSA acceleration is reported in Fig. 1.3

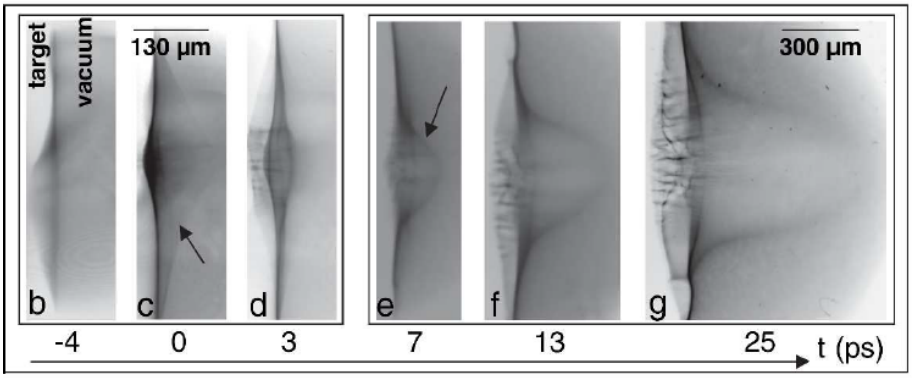

Figure 1.3: Proton probing of the expanding sheath at the target rear surface. The temporal series of images are produced by the deflection of probe protons passing through the TNSA field in a time-of-flight arrangement [14]

The following experimentally verified relation shows the maximum ion energy ε_{max}, as a function of the laser intensity I_L and laser pulse energy E_L [22]:

$$\varepsilon_{max} = Zm_ec^2 \left[\left(1 + \frac{I_L\lambda^2}{1,38 \cdot 10^{18}} \right)^{\frac{1}{2}} - 1 \right] (4,8 + 0,8 \ln[E_L(J) - 1]) \,. \tag{1.25}$$

There is also a possibility to get two accelerated proton beams in different directions. In fact the ion beam direction is mainly perpendicular to the target normal but using wedge targets it can be controlled, as reported in [14].

In [22] 100 MeV protons in TNSA regime are predicted using laser pulse with the following characteristics: $\tau_L = 25$ fs (pulse duration), $f_L = 3$ μm (focal spot), $\lambda = 0,8$ μm (laser wavelength), $E_L \approx 5,5$ J (pulse energy) and $I_L\lambda^2 \approx 2 \cdot 10^{21}$ (W/cm^2)μm^2 (pulse irradiance). This gives great expectations in future applications and in particular for hadrontherapy as it will be discussed later on.

1.4 Other acceleration regimes – Radiation Pressure Acceleration (RPA)

Another acceleration mechanism is the Radiation Pressure Acceleration (also known as "Laser piston regime") which occurs at the target front surface The RPA is based on the radiation pressure which accelerates the whole foil as a plasma slab. The radiation pressure has its origin in the electromagnetic waves which carry a momentum. This momentum can be transferred to a non-transparent (reflecting/absorbing) suface which is hit by the waves.
This idea was first published by Maxwell in his theory of electromagnetism. The relation for radiation pressure is given by:

$$P_{rad} = \frac{\langle \vec{S} \rangle}{c}, \tag{1.26}$$

where $\langle \vec{S} \rangle$ is the time averaged energy flux density given by the Pointing vector $\vec{S} = \vec{E} \times \vec{H}$, where $\vec{H}$ is magnetic field strength and $\vec{E}$ is electric field. P_{rad} must be multiplied by a factor of 2, if the wave is completely reflected [38].
The radiation pressure is related to the total steady ponderomotorive force on the medium. The electrons of overdense plasma are pushed inwards by PF and leave the dielectric layer. This creates an electrostatic field which finally leads to acceleration.
Simulations predict that the RPA regime can be very efficient and can provide higher ion energies than TNSA [17]. However, the requirements for effective RPA such as circular polarization, ultrahigh intensity and high contrast of the laser pulse, currently do not make this acceleration regime easily accessible [12].

1.5 Scaling laws for laser-accelerated proton beams

In this subchapter we will discuss some basic scaling laws for laser-accelerated proton beams. In Fig. 1.4 we report two graphs from [26]. In the left one, the behaviour of electric field ratio on z/λ_D ratio is shown, where λ_D is the Debye length and z is the ion trajectory along the axis. The right one shows the ion kinetic energy dependence on time. Moreover, we can see that to accelerate protons up to 100 MeV, it is necessary to hold the plasma at the same temperature for approximately 650 fs. This was, and still is, one of the major problems of generating such energetic protons [26]. For both graphs, the scaling lines assume a constant field and an isothermal model.
A very interesting scaling law study is reported in [5], where experimental results obtained with Al foils are discussed. The proton-beam maximum energy and energy-conversion efficiency are measured with various targets and laser parameters. For these experiments, the rear surface acceleration mechanism 1.2.1 was chosen.

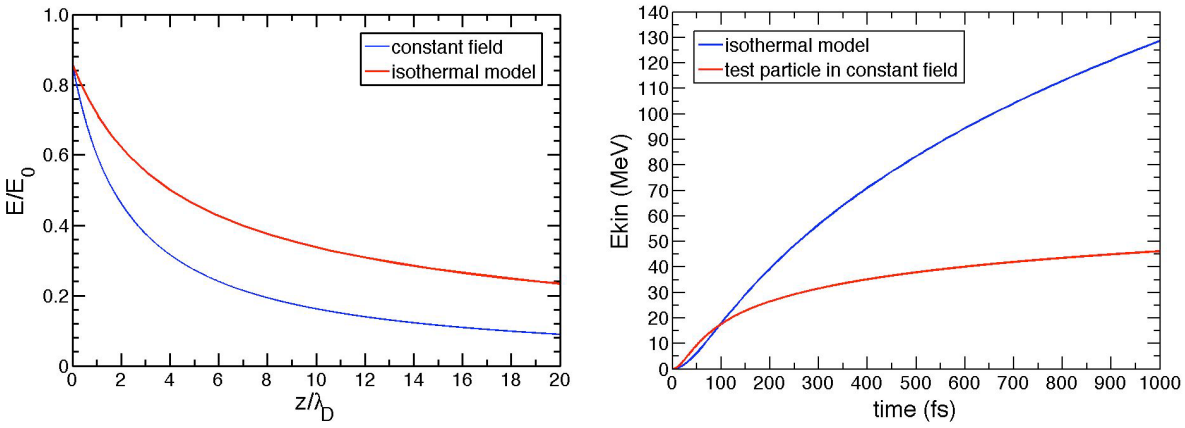

Figure 1.4: Left: E/E_0 ratio dependence on z/λ_D ratio, where E and E_0 is the actual and the rest electric field, z is the trajectory along the z axis and λ_D is the Debye length; Right: kinetic energy dependence on time scale; [26]

The maximum proton energy (under assumption of isothermal fluid model [5]) follows the equation:

$$E_{max} = 2T_{hot}\left[\ln(t_p + \sqrt{t_p^2+1})\right]^2, \tag{1.27}$$

where $t_p = \omega_p t_{acc}/\sqrt{2\exp(1)}$ is the normalized acceleration time with plasma frequency defined as $\omega_p = \sqrt{Z_i e^2 n_{e0}/(m_i \varepsilon_0)}$ (for clarity we note that e is the elementary charge, t_{acc} is acceleration time, ε_0 is electric permittivity, m_i is mass of particle and Z_i is charge number; for protons $m_i = m_p$ and $Z_i = 1$), n_{e0} is the density and T_{hot} is the temperature of hot electrons, discussed in 1.0.2, which are crucial for rear surface acceleration mechanism, discussed in 1.2.1. Also, as we have already discussed, preplasma may be generated at the target front side.
The first scaling law is reported in Fig. 1.5. When the target thickness decreases, the maximum proton energy and energy conversion efficiency grows. But if the target is too thin (8μm for parameters of the exp. in Fig. 1.5) the proton energy drops down because of the rear surface disruption. Further details are reported in [5].
The experimentally confirmed relation between the effective acceleration time t_{acc} and laser pulse duration τ_{laser} is [5]:

$$t_{acc} \sim 1,3 \quad \tau_{laser}. \tag{1.28}$$

A study of the proton beam energy characteristics against the laser energy (when laser pulse duration τ_{laser} is constant) is shown in Fig. 1.6. The proton beam energy characteristic dependence on laser pulse duration, when the laser intensity stays constant is reported in Fig. 1.7. Fig. 1.6(b) graph demonstrates that the energy conversion efficiency increases more with the laser energy than the laser energy does with the constant laser pulse duration. The reason is simple. With the laser energy growth, the proton spectrum reaches the higher energies and also the number of particles grows. In other words, from the proton beam we get more energy when we use one 10 J shot than ten ones at 1 J.

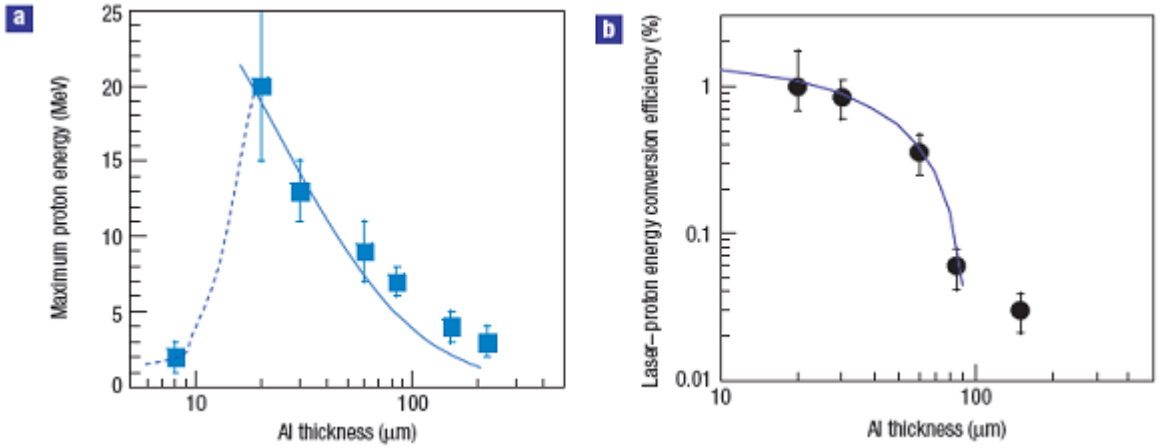

Figure 1.5: *Thinner solid targets improve the maximum energy of laser-accelerated protons as well as the laser-proton energy conversion efficiency.* (a): Maximum proton energy, and (b): laser-proton energy conversion (calculated for protons with energy > 4 MeV) for similar laser conditions ($\tau_{lase} = 320$ fs and $I \sim 4{\cdot}10^{19}$ W cm^{-2}) and various Al foil thicknesses. Data points represent experimental data and solid lines calculations using the fluid model with the same laser parameters; [5].

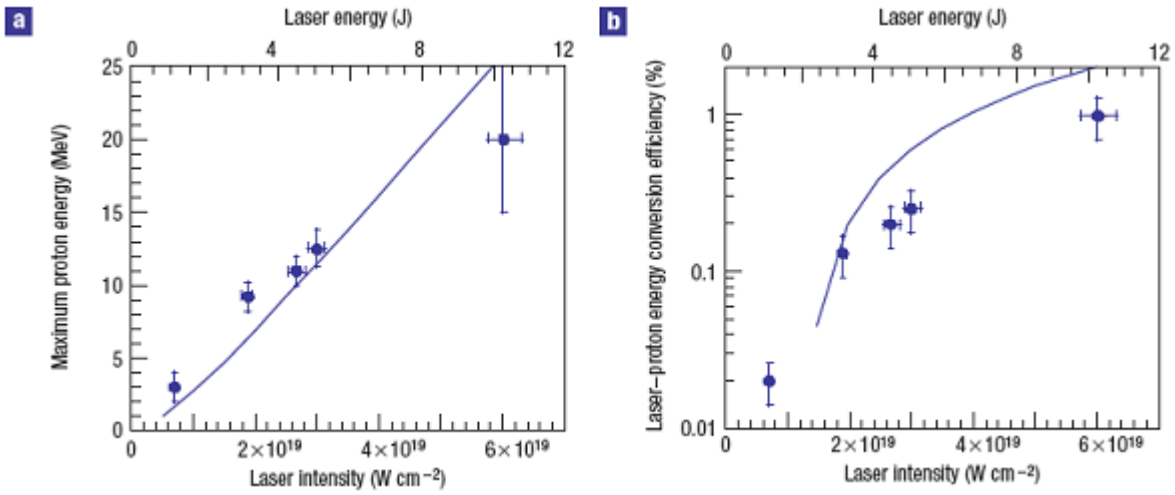

Figure 1.6: *The laser-accelerated proton maximum energy and conversion efficiency increase with the pulse energy.* (a): Maximum energy of proton beam and (b): laser-proton conversion efficiency (for protons with energy > 4 MeV) as a function of the laser intensity (bottom axis) and the laser energy in the focal spot (top axis). The laser pulse duration is constant at 320 fs.The lines in (a) and (b) are calculations using the fluid model with the actual laser parameters; [5].

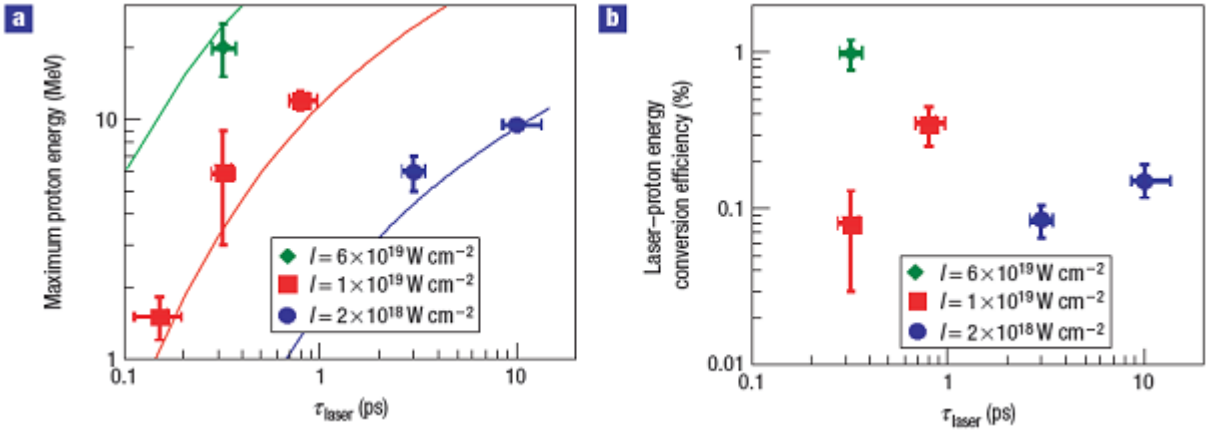

Figure 1.7: *Longer pulses improve the laser-accelerated proton maximum as well as the energy conversion efficiency.* (a): Maximum energy of the proton beam and (b): laser-proton energy conversion efficiency (for protons with energy > 4 MeV) as a function of the laser pulse duration for three different laser intensities; the laser energy is increased with the laser pulse duration to keep the laser intensity constant for each group of points. The lines are calculations for each intensity using the fluid model; [5].

Chapter 2

Behaviour of charged particle beams in a solenoid magnetic field

2.1 Characteristics of a solenoid magnetic field

2.1.1 Introduction

We can separe the solenoid magnetic field into two components – longitudinal and radial. The longitudinal magnetic field B_z reaches on axis from zero to its maximum value in the middle of the solenoid. By contrast, the radial component of the solenoid magnetic field B_r has its maximum amplitude at the two ends of the solenoid. To make it simple, the assumption of uniform field inside the solenoid and zero field intensity outside is usually used [8]. This behaviour is clearly shown in Fig. 2.1; [11]. A more detailed description of the magnetic field is reported in 2.2.

2.1.2 Larmour radius and Larmour frequency

When a particle enters the solenoid magnetic field it begins to rotate. The movement of a charged particle in a homogenous magnetic field is called the Larmuor rotation [37] and the particle circumscribes a circle or helix path. Evidently, the force acting on an elementary particle in a magnetic field $\vec{B}$ moving with the velocity $\vec{v}$ can be expresed by the Lorentz equation $\vec{F} = \vec{v} \times \vec{B}$. The particle velocity can be separated into two components according to the magnetic field direction – perpendicular $v_\perp$ and parallel velocity $v_\parallel$.
By using the Lorentz equation we will get two terms with different velocities $\vec{v_\parallel}$ and $\vec{v_\perp}$: $\vec{F} = e\vec{v_\perp} \times \vec{B} + e\vec{v_\parallel} \times \vec{B}$. Due to the cross product the second term is 0, because $\vec{B}$ and $\vec{v_\parallel}$ have the same direction. Thus, in the field's direction there is no force. When $\vec{v_\parallel} = 0$ particle circumscribes a circle without forward movement. If $\vec{v_\parallel} \neq 0$ the particle is moving with constant speed forward on a helix. The first term causes a circular trajectory, because a component of magnetic force $F_m = eBv_\perp$ is perpendicular to the velocity, so it acts as a centrifugal force

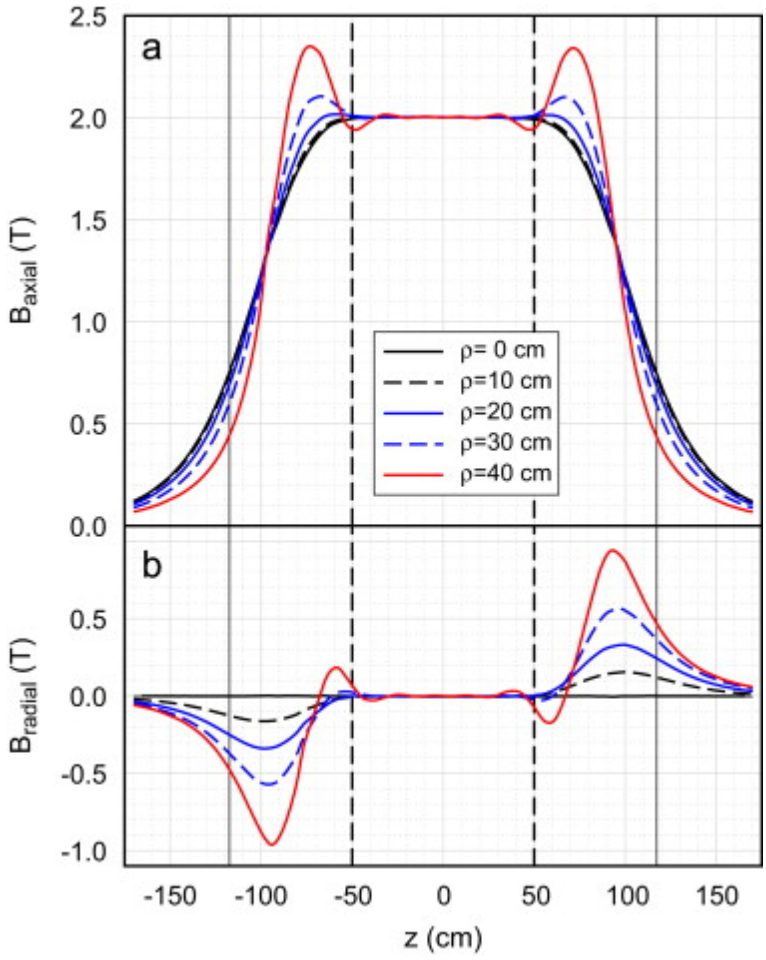

Figure 2.1: Axial (a) and radial (b) components of a magnetic field; ρ – different distances from the solenoid axis; The vertical dashed lines indicate the region of highest field uniformity; [11]

F_c, thus:

$$F_m = F_c, \tag{2.1}$$

$$eBv_\perp = \frac{mv_\perp^2}{r} \qquad \Rightarrow \qquad r = \frac{mv_\perp}{eB}, \tag{2.2}$$

$$T_c = \frac{s}{v_\perp} = \frac{2\pi r}{v_\perp} = \frac{2\pi m}{eB} \qquad \Rightarrow \qquad \omega_c = \frac{2\pi}{T_c} = \frac{eB}{m}, \tag{2.3}$$

where e is elementary charge, m is mass of the particle, s is trajectory length, r is radius of the circle trajectory, T_c is time period and ω_c is cyclotron frequency bounded with time period by relation $\omega_c = 2\pi/T_c$. In the relativistic cases we have to add the relativistic gamma factor to the mass:

$$\omega_c = \frac{eB}{\gamma m}. \tag{2.4}$$

The relation for the Larmour frequency is [8]:

$$\omega_L = \frac{1}{2}\omega_c = \frac{eB}{2\gamma m}. \tag{2.5}$$

The difference between the Larmour and cyclotron frequency consists in the used geometry. Particles rotate around the centre of their own trajectories with the cyclotron frequency (2.3) but with the Larmour frequency (2.5) around the solenoid axis. This is simply ilustrated in Fig. 2.2.

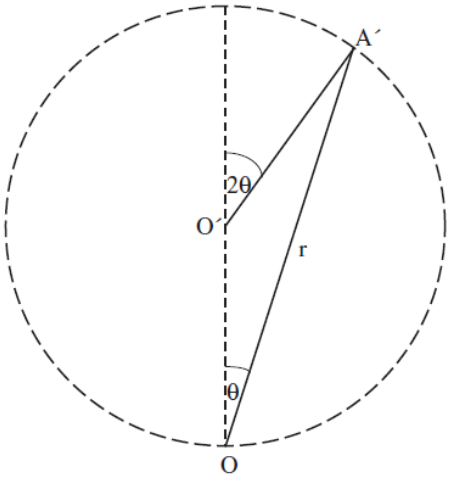

Figure 2.2: Geometric explanation of the relation between the Larmour and the cyclotron frequency; O – point on the solenoid axis, O' – centre of the individual circular trajectory, A' – location of the particle; [8]

With transverse velocity $\vec{v_\perp}$ the particle moves on a helix with a constant radius called the Larmour radius R_L ($\vec{v_\parallel} = 0$, so $\vec{v_\perp}$ is velocity of the particle $\vec{v_\perp} = \vec{v}$):

$$R_L = \frac{v_\perp}{\omega_L} = \frac{\gamma m v_\perp}{eB}. \tag{2.6}$$

2.1.3 Axisymetric solenoid magnetic field relations

Magnetic field of a solenoid

Far from the ends of the solenoid the Ampere's Law [31] can be used to calculate the field strength, because $\vec{B}$ has a uniform value inside the solenoid and $|\vec{B}| = 0$ outside (as mentioned in 2.1.1). For getting the enclosed current in loop from the Ampere's Law we can use the relation:

$$I_{en} = InL, \tag{2.7}$$

where n is the number of coils per meter, L is the loop length and I is the current through the wire. We obtain the final relation for the magnetic field intensity by using (2.7) and the Ampere's

Law:

$$\oint \vec{B}\mathrm{d}\vec{l} = \mu_0 \iint_S \vec{J}\mathrm{d}\vec{S} = \mu_0 I_{en}, \tag{2.8}$$

$$\oint \vec{B}\mathrm{d}\vec{l} = BL \quad \Rightarrow \quad B = \frac{1}{L}\mu_0 I_{en}, \tag{2.9}$$

$$B = \mu_0 n I. \tag{2.10}$$

Magnetic field along the solenoid axis

Sometimes we need the relation for the magnetic field along the axis. In this case we cannot use the Ampere's Law as in section 2.1.3, because the field is not uniform anymore. Instead, we will follow the principle of superposition in two steps. Firstly, we will consider little increase of $\mathrm{d}\vec{B}$ which equals one ring of a current and secondly, integrate over all coils to gain the total $\vec{B}$.
If we use the Biot-Savart Law [33] and realize that the radial component of the magnetic field will be cancelled, then the horizontal component $\mathrm{d}B_z$ can be written as follows [25]:

$$\mathrm{d}\vec{B} = \frac{\mu_0 I}{4\pi}\frac{\mathrm{d}\vec{l}\times\hat{r}}{r^2}, \tag{2.11}$$

$$\mathrm{d}B_z = \mathrm{d}\vec{B}\sin\theta = \frac{\mu_0 I}{4\pi}\frac{\mathrm{d}s}{r^2}\frac{R}{r} = \frac{\mu_0 I}{4\pi}\frac{\mathrm{d}sR}{(R^2+D^2)^{3/2}}, \tag{2.12}$$

where $\hat{r}$ is the unit vector of $\vec{r}$, μ_0 is the vacuum permeability constant and I is a steady current in a loop which generates the magnetic field B. Meaning of other symbols are explained in Fig. 2.3.

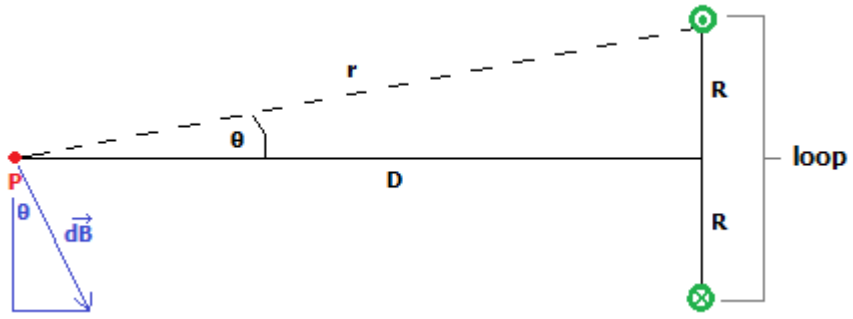

Figure 2.3: Geometry for deriving B_z from Biot-Savart Law; P – the point from which we calculate the magnetic field, R – the radius of the coil, D – the distance from point P to the loop, θ – the angle, r – the distance from P to the top of the loop

The reason why the radial components of the magnetic field are cancelled out is simple; the coil wire of radius R carries the current I and creates the magnetic field in point P. The magnetic field on the top of the loop points down (coordinate r) and right (coordinate z), but at the bottom of the loop it points up and right.

Now we will integrate $\mathrm{d}B_z$ over all segments of the loop:

$$B_z = \int_{loop} \mathrm{d}B_z = \frac{\mu_0 I}{4\pi} \frac{R}{(D^2+R^2)^{3/2}} \int_{loop} \mathrm{d}s, \tag{2.13}$$

$$B_z = \frac{\mu_0 I}{2} \frac{R^2}{(D^2+R^2)^{3/2}}, \tag{2.14}$$

but we have to keep in mind that this is only a z-magnetic field along the axis for one single loop. Then we have to get the relation for all loops.
Firstly, we get a small part of length $\mathrm{d}x$ (as shown in Fig. 2.4) considering the current I and n as the number of turns per unit length. The relation for the total current in this section is:

$$I_{tot} = In\mathrm{d}x = I\frac{N}{L}\mathrm{d}x. \tag{2.15}$$

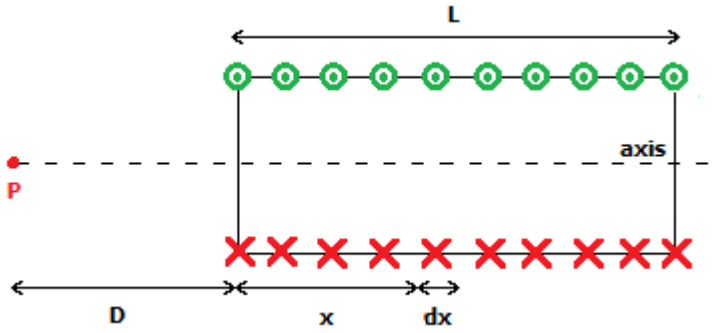

Figure 2.4: The position of the solenoid due to the position of the measurement point P

When the section is located at a distance $D + x$ from the point P, the relation (2.14) can be rewritten this way:

$$B_z = \frac{\mu_0 In\mathrm{d}x}{2} \frac{R^2}{((D+x)^2+R^2)^{3/2}}. \tag{2.16}$$

Moreover, the total value of the magnetic field we reach by integrating over the length of the solenoid is:

$$B_{z_{tot}} = \int_{length} B_z = \frac{\mu_0 InR^2}{2} \int_0^L \frac{\mathrm{d}x}{((D+x)^2+R^2)^{3/2}}, \tag{2.17}$$

after substitutions $D + x = z$ and $z = \tan u$ we finally get the result:

$$B_{z_{tot}} = \frac{\mu_0 In}{2} \left(\frac{D+L}{\sqrt{(D+L)^2+R^2}} - \frac{D}{\sqrt{(D)^2+R^2}} \right), \tag{2.18}$$

which can be rewritten as:

$$B_{z_{tot}} = \frac{\mu_0 In}{2} \left(\frac{x_2}{\sqrt{x_2^2+R^2}} - \frac{x_1}{\sqrt{x_1^2+R^2}} \right), \tag{2.19}$$

where x_1 and x_2 are distances (on axis) from the ends of the solenoid to the magnetic field measurement point P.
In the case that the measurement point P is located (on axis) in the centre of the solenoid ($x_1 = -x_2$):

$$B_{z_c} = \frac{\mu_0 In}{2}\left(\frac{x_2}{\sqrt{x_2^2+R^2}} + \frac{x_2}{\sqrt{x_2^2+R^2}}\right) = \frac{\mu_0 nI}{\sqrt{1+\left(\frac{R}{x_2}\right)^2}}. \tag{2.20}$$

Because the measurement point P is located in the centre, the relation $L = 2x_2$ is valid. Finally, the relation for the on-axis magnetic field B_z measured in the centre of the solenoid is given by:

$$B_{z_c} = \frac{\mu_0 nI}{\sqrt{1+\left(\frac{R}{x_2}\right)^2}} = \frac{\mu_0 NI}{\sqrt{L^2+\left(L\frac{R}{x_2}\right)^2}}, \tag{2.21}$$

$$B_{z_c} = \frac{\mu_0 NI}{\sqrt{L^2+4R^2}}. \tag{2.22}$$

2.2 Beam dynamics in a solenoid

Along this section we will assume the following [8]:

- warm beam – no Coulomb repulsion between charged particles
- cold beam – the initial transverse velocity of particle is zero

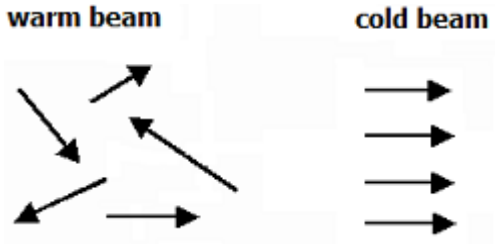

Figure 2.5: Directions of initial velocities for warm and cold beam

2.2.1 Magnetic field according to z coordinate

The spatial arrangement of the solenoid can be composed of three regions according to the z coordinate. We will describe the characteristics of the field, the trajectory of particles etc. for each region or for boundary between them in seperate paragraphs for better clarity. Components of the magnetic field can be expressed by [8]:

$$B_z = B_0\left[u(z) - u(z-L)\right], \tag{2.23}$$

$$B_r = -\frac{r}{2}B_0\left[\delta(z) - \delta(z-L)\right], \tag{2.24}$$

where L is the length of the solenoid; $u(z) = 1$ for $z > 0$ and $z = 0$ otherwise and $\delta(z)$ is a Dirac delta function. Consequently, the $B_z = B_0$ for $0 < z < L$ and $B_z = 0$ otherwise.

region 1 ($z < 0$)

- field-free region
- straight trajectory
- equations for velocity components:

$$v_r = 0, \tag{2.25}$$
$$v_\theta = 0, \tag{2.26}$$
$$\text{initial } v_z \tag{2.27}$$

boundary between 1^{st} region and 2^{nd} region ($z = 0$)

We have to connect the trajectories of 1^{st} and 2^{nd} region together. Radial component of the magnetic field (2.24) gives an azimuthal impulse with the Lorentz force $F = -ev_z B_r(z)$. Because of the impulse we will notice an increase in azimuthal velocity v_θ. This increment is given by:

$$\Delta v_\theta = r_0 \omega_L, \tag{2.28}$$

where ω_L is the Larmour frequency (2.5) and r_0 is the radial coordinate of the particle when it enters 2^{nd} region. The radial component of the velocity v_r remains steady when enters from 1^{st} to 2^{nd} region. So, $v_r = 0$ in $z = 0$. The change in the third component of $\vec{v}$, longitudinal velocity v_z, is neglected because of the paraxial approximation (for more details see [8]).

region 2 ($0 < z < L$)

- uniform magnetic field
- helical trajectory with the radius R_c:

$$R_c = \frac{\gamma m v_\perp}{eB_0} = \frac{r_0}{2}. \tag{2.29}$$

  This means that the non-axis particle rotates on the helix with a radius which corresponds to half of its initial radial displacement from the solenoid axis.

- The velocity of motion on a helix can be decomposed into radial and azimuthal components, the longitudinal component of particle's velocity is caused by forward movement. The equations for velocity components are:

$$v_r = -r\omega_L \tan\left(\frac{\omega_L z}{v_z}\right), \tag{2.30}$$
$$v_\theta = r\omega_L, \tag{2.31}$$
$$v_z \text{ same as in } 1^{st} \text{ region} \tag{2.32}$$

  and r is given by $r = r_0 \cos\left(\frac{\omega_L z}{v_z}\right)$.

- the particle undergoes the periodic focusing (chapter 2.2.2)

boundary between 2^{nd} region and 3^{rd} region ($z = L$)

For the radial component of the magnetic field the relation (2.24) is valid. The Lorentz force, as in the boundary between 1^{st} and 2^{nd} region, gives an impulse in azimuthal direction. Similarly the change in v_θ is given by:

$$\Delta v_\theta = -r_1 \omega_L, \tag{2.33}$$

where r_1 is the radial coordinate of the particle when it exits 2^{nd} region.

region 3 ($z > L$)

- field-free region
- straight trajectory
- equations for velocity components:

$$\text{constant} \qquad v_r = -r_1 \omega_L \tan\left(\frac{\omega_L L}{v_z}\right), \tag{2.34}$$

$$v_\theta = 0, \tag{2.35}$$

$$v_z \text{ same as in } 1^{st} \text{ and } 2^{nd} \text{ region} \tag{2.36}$$

  We can get relation 2.35 from relations 2.32 and 2.33.

- particle can be ideally focused to a point

2.2.2 Focusing of charged particle beams in a solenoid magnetic field

For the sake of explanation of focusing in the 2^{nd} region, we will use a simple geometric picture Fig. 2.6, which shows a cross-section (or trajectory projection – it depends if the particles have forward motion) of the beam as it enters the second region.

We will assume that our beam (a solid circle in the picture) has four particles – A, B, C, D, situated on the beam surface (or, if speaking about the cross-section, on the beam periphery). Each particle moves on a circular trajectory in the $x - y$ plane which is depicted by dotted lines. Moreover each particle touches the solenoid axis just once and returns to its circular trajectory. After some time and a certain distance the particles move on their trajectories to new spots. The new positions of the particles are marked as A', B', C', D'. For better understanding there is also a particle E which is not situated on the beam surface at the beginning and its new position E' is in the volume of the new *focused* beam shown as a dashed circle. The radius of the original beam decreases from OA to OA'. This is the main process of periodic focusing in the 2^{nd} region with a uniform magnetic field.

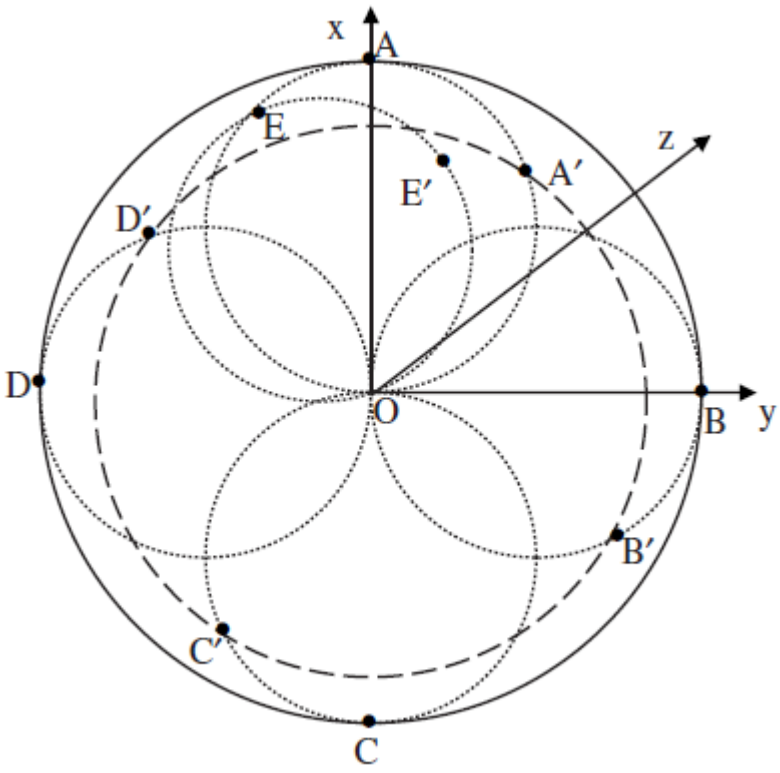

Figure 2.6: Focusing in the region with a uniform magnetic field; A, B, C, D, E – particles' positions at the beginning, A', B', C', D', E' – particles' positions after focusing, O – the centre of the beam; [8]

2.3 Magnetic field transformation into cylindrical coordinates

In this section we will explain the cylindrical coordinate system transformation and show how to transform equations of the motion of particles in solenoid and solenoid magnetic field from cartesian coordinates.

2.3.1 Cylindrical coordinate system, velocity, acceleration

The cylindrical coordinate system has three dimensions and in contrast with the cartesian one, the description contains an angle. The main transformation relation between the cartesian coordinates (x, y, z) and the cylindrical coordinates (r, θ, z) is given by:

$$\vec{r} = \begin{pmatrix} x \\ y \\ z \end{pmatrix} = \begin{pmatrix} r\cos\theta \\ r\sin\theta \\ z \end{pmatrix}. \tag{2.37}$$

From Fig. 2.7 it is clear that r, θ, z can by expressed by x, y, z:

$$r = \sqrt{x^2 + y^2}, \qquad \theta = \arctan(y/x), \qquad z = z. \tag{2.38}$$

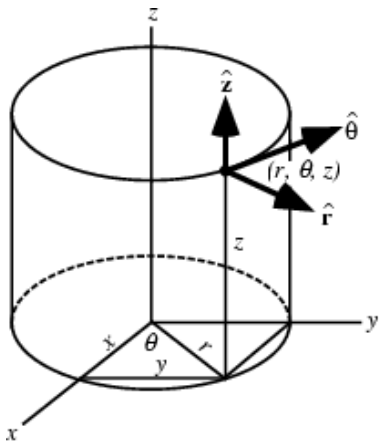

Figure 2.7: Geometry of cylindrical and cartesian coordinate systems; [7]

Any vector can be made into a unit vector by dividing it by its length. With the hat we will denote these unit vectors and a unit angle [7]:

$$\hat{\vec{r}} = \frac{\frac{\mathrm{d}\vec{r}}{\mathrm{d}r}}{\left|\frac{\mathrm{d}\vec{r}}{\mathrm{d}r}\right|} = \begin{pmatrix} \frac{\mathrm{d}(r\cos\theta)}{\mathrm{d}r} \\ \frac{\mathrm{d}(r\sin\theta)}{\mathrm{d}r} \\ \frac{\mathrm{d}z}{\mathrm{d}r} \end{pmatrix} = \begin{pmatrix} \cos\theta \\ \sin\theta \\ 0 \end{pmatrix}, \tag{2.39}$$

$$\hat{\theta} = \frac{\mathrm{d}\vec{r}}{\mathrm{d}\theta} = \begin{pmatrix} \frac{\mathrm{d}(r\cos\theta)}{\mathrm{d}\theta} \\ \frac{\mathrm{d}(r\sin\theta)}{\mathrm{d}\theta} \\ \frac{\mathrm{d}z}{\mathrm{d}r} \end{pmatrix} = \begin{pmatrix} -\sin\theta \\ \cos\theta \\ 0 \end{pmatrix}, \tag{2.40}$$

$$\hat{\vec{z}} = \frac{\frac{\mathrm{d}\vec{r}}{\mathrm{d}z}}{\left|\frac{\mathrm{d}\vec{r}}{\mathrm{d}z}\right|} = \begin{pmatrix} \frac{\mathrm{d}(r\cos\theta)}{\mathrm{d}z} \\ \frac{\mathrm{d}(r\sin\theta)}{\mathrm{d}z} \\ \frac{\mathrm{d}z}{\mathrm{d}z} \end{pmatrix} = \begin{pmatrix} 0 \\ 0 \\ 1 \end{pmatrix}. \tag{2.41}$$

Now we have everything to derive velocity and acceleration in the cylindrical coordinates:

$$\dot{r} = \frac{\mathrm{d}\vec{r}}{\mathrm{d}t} = \frac{\mathrm{d}}{\mathrm{d}t}\begin{pmatrix} r\cos\theta \\ r\sin\theta \\ z \end{pmatrix} = \dot{r}\hat{\vec{r}} + r\dot{\theta}\theta_0 + \dot{z}\hat{\vec{z}}, \tag{2.42}$$

$$\ddot{r} = \frac{\mathrm{d}\dot{r}}{\mathrm{d}t} = (\ddot{r} - r\dot{\theta}^2)\hat{\vec{r}} + (2\dot{r}\dot{\theta} + r\ddot{\theta})\hat{\theta} + \ddot{z}\hat{\vec{z}}. \tag{2.43}$$

2.3.2 Cylindrical magnetic field $\vec{B}$ in a solenoid

The solenoid magnetic field has three components $\vec{B} = (B_r, B_\theta, B_z)$. The field is axially symetric, which means that there is no angle dependence. For that reason we can consider:

$$B_\theta = 0. \tag{2.44}$$

For derivating B_z we will use the Taylor series for $(1+x)^r$ [41]. So, if $r \in \mathbf{R}$ and $x \in (-1;1)$:

$$(1+x)^r = 1 + \binom{r}{1}x + \binom{r}{2}x^2 + \binom{r}{3}x^3 + \ldots = \sum_{n=0}^{\infty}\binom{r}{n}x^n. \tag{2.45}$$

Then, we can derivate B_z using (2.44), premise $B_r \ll B_z$ (so $\frac{B_r}{B_z} = x \in (-1;1)$) and (2.45):

$$B = \sqrt{B_r^2 + B_z^2 + B_\theta^2}, \tag{2.46}$$

$$B = \sqrt{B_r^2 + B_z^2} = B_z\sqrt{1 + \left(\frac{B_r}{B_z}\right)^2} \simeq B_z\left[1 + \frac{1}{2}\left(\frac{B_r}{B_z}\right)^2 + ...\right] \simeq B_z + \frac{1}{2}\frac{B_r^2}{B_z}, \tag{2.47}$$

$$B_z \simeq B \equiv B_0, \tag{2.48}$$

$$B_z = B_0, \tag{2.49}$$

where the original magnetic field has been marked as B_0.
For deriving the B_r we use Gauss's Law for magnetism and the relation for nabla in cylindrical coordinates [35]:

$$\nabla \cdot \vec{B} = 0, \tag{2.50}$$

$$\nabla \cdot \vec{B} = \frac{1}{r}\frac{\partial(rB_r)}{\partial r} + \frac{1}{r}\frac{\partial B_\theta}{\partial \theta} + \frac{\partial B_z}{z}, \tag{2.51}$$

$$\frac{\partial r B_r}{\partial r} = -r\frac{\partial B_z}{\partial z}, \tag{2.52}$$

$$rB_r = -\int r\frac{\partial B_z}{\partial z}\mathrm{d}r = -\frac{r^2}{2}\frac{\partial B_z}{\partial z}, \tag{2.53}$$

$$B_r = -\frac{r}{2}\frac{\partial B_z}{\partial z}. \tag{2.54}$$

Then, the final relation for the solenoid magnetic field:

$$\vec{B} = (B_r, B_\theta, B_r) = (-\frac{r}{2}B_0', 0, B_0), \tag{2.55}$$

where B_0 is the value of the original magnetic field and comma means derivative with respect to z.

2.3.3 Derivation of equations of motion in cylindrical coordinates

The Lorentz force is acting on a particle located in a magnetic field. For deriving cylindrical equations of motion the force transformation is needed [7]:

$$\vec{F} = m\vec{a} = m\ddot{\vec{r}} = e\vec{v} \times \vec{B} = e\dot{\vec{r}} \times \vec{B} = e\begin{vmatrix} \hat{\vec{r}} & \hat{\theta} & \hat{\vec{z}} \\ \dot{r} & r\dot{\theta} & \dot{z} \\ B_r & B_\theta & B_z \end{vmatrix}. \tag{2.56}$$

Then, if we use (2.43):

$$m\left((\ddot{r}-r\dot{\theta}^2)\hat{\vec{r}}+(2\dot{r}\dot{\theta}+r\ddot{\theta})\hat{\theta}+\ddot{z}\hat{\vec{z}}\right)=e\left((r\dot{\theta}B_z-\dot{z}B_z)\hat{\vec{r}}+(r\dot{z}B_r-\dot{r}B_z)\hat{\theta}+(\dot{r}B_\theta-r\dot{\theta}B_r)\hat{\vec{z}}\right). \tag{2.57}$$

The equations of motion in cylindrical coordinates are finally acquired by comparing coefficients of unit vectors $\hat{\vec{r}}, \hat{\theta}$ and unit angle $\hat{\vec{z}}$ in (2.57):

$$m(\ddot{r}-r\dot{\theta}^2)=er\dot{\theta}B_z \qquad \text{focusing,} \tag{2.58}$$

$$m(2\dot{r}\dot{\theta}+r\ddot{\theta})=e(\dot{z}B_r-\dot{r}B_z) \qquad \text{rotation,} \tag{2.59}$$

$$m\ddot{z}=-er\dot{\theta}B_r \qquad \text{acceleration.} \tag{2.60}$$

2.4 Emittance

Each particle at any point along the beam transport line is characterized by a point in six-dimensional phase space described by coordinates $(x, p_x, y, p_y, \sigma, E)$, where for transverse momenta the relations $p_x \approx p_0 x'$ and $p_y \approx p_0 y'$ are valid, $cp_0 = \beta E_0$, E_0 is the ideal particle energy, E is the particle energy and σ is the coordinate along the trajectory. The coupling between vertical and horizontal plane can be repaired in two ways – ignoring coupling in linear beam dynamics or treating it as a perturbation. Then it is possible to split the six-dimensional phase space into three independent two-dimensional planes [30] and derive the equations of motion in each plane separately, as will be done in 2.4.2.
For this reason we can speak about three independent beam emittances with two dimensions. The emittance is a parameter of the beam which characterizes its size. Examples of beam emittance are shown in Fig. 2.8. In the left picture there are particles appearing from a disk (having radius w) and straight trajectories under an angle of $\pm 90°$, where this angle is measured from the disk's surface. As depicted in the picture, the particles have a large distribution of transverse momenta. In the right picture the limitations by an aperture are shown. For a simpler explanation, the aperture has the same radius as the source and is located at distance d from the source. A certain amount of particles will be absorbed at the iris. Those which will pass through will occupy the phase space area shaded on the right picture noted as "phase space representation".
We use the emittance for describing the beam, since it is invariant in absence of dissipative or cooling forces. This means that the beam occupies a constant volume in the phase space or a certain region in phase plane, respectively. This is actually what Liouville's theorem claims. Moreover we can prove that in the phase space the particle density does not change along the beam transport line. Due to this fact, the forces acting on a particle can be derived from macroscopic electric and magnetic fields. Furthermore, from knowledge of an occupied area in phase space we are able to reach the location and distribution of the beam at any place along the transport line, thus knowledge of the trajectories of every individual particle is not necessary. In other words, it is possible to describe the collective behaviour of the beam by the properties of a single particle.
The invariant (emittance) can be expressed as:

$$\varepsilon = \gamma x^2 + 2\alpha x x' + \beta x'^2, \tag{2.61}$$

where α, β, γ are Twiss parameters (discused in 2.4.1).

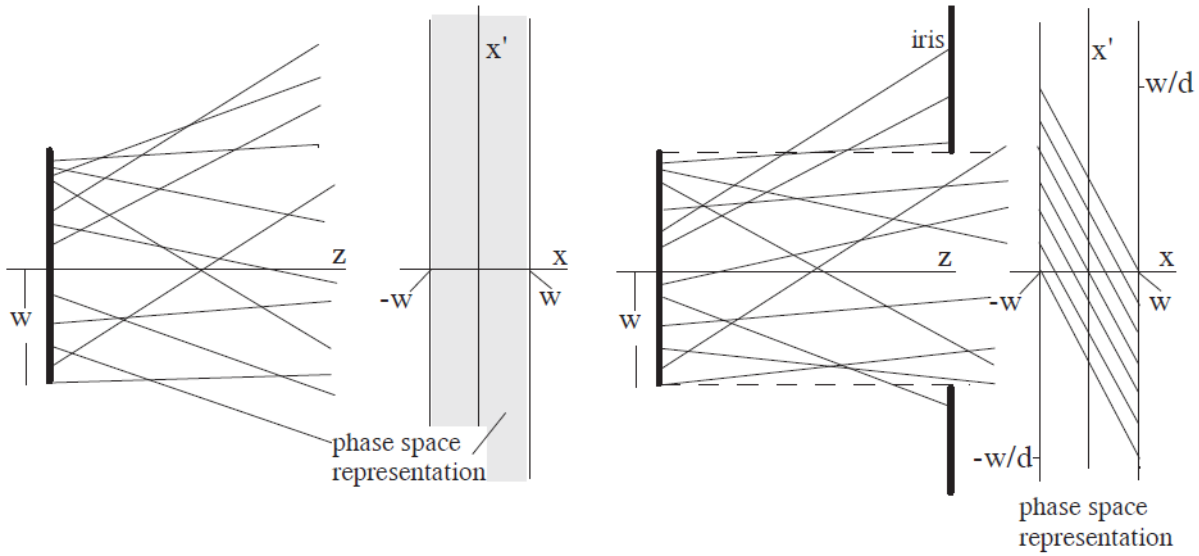

Figure 2.8: Beam from a diffuse source in coordinate space and in the phase space (left). Reduction of phase space (shaded area) due to beam restriction by an iris aperture (right); [30]

The equation (2.61) is an expression of an ellipse called phase or emittance ellipse (see Fig. 2.10), which surrounds all the particles of the beam in the phase space (Twiss parameters determine its shape and orientation). The area enclosed by this ellipse is called beam emittance also expressed as:

$$\int_{ellipse} \mathrm{d}x\mathrm{d}x' = \pi\varepsilon, \tag{2.62}$$

which means, that the numerical value of the emittance multiplied by π is equal to the phase space region of the beam. All particles travel along their individual ellipses in the phase space (further details in [30]).
We can also take a look at focusing from the emittance point of view. The phase ellipse in the drift space can be pushed to the right without changing the angular envelope i.e. $A = x'_{max} = \sqrt{\varepsilon\gamma}$ stays constant. Naturally, if the drift space is long enough it is possible that a convergent beam can change into a divergent one as we can see in Fig. 2.9.
The beam behaviour can be characterized by the form and orientation of the beam ellipse. A convergent beam can be recognized by the rotated phase ellipse in position from 2^{nd} (left upper) to 4^{th} (right lower) quadrant and divergent beam as the ellipse from 1^{st} (right upper) to 3^{rd} (left lower) quadrant. The upright position (symmetric) means location of waist or symmetry point (more in [30]).
The cause of the finite emittance is the nonzero ion temperature. Finally, we only mention some other factors that affect the beam emittance [44]:

- the intrinsic energy distribution of particles in the ion source,
- the spatial and angular distribution of particles in the ion source,
- the aberration of beam transport and acceleration components,

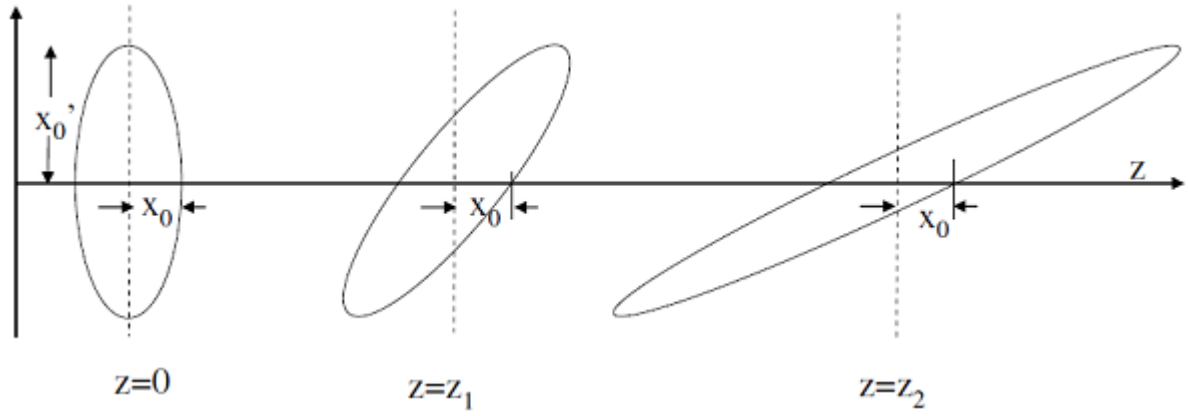

Figure 2.9: Transformation of a phase space ellipse at different locations along a drift section; [30]

- the space charge force (mutual electrostatic repulsion),
- the beam quality degraders (foil stripper, charge exchange cell...),
- bad vacuum.

2.4.1 Twiss parameters

A single particle position x can be described as a function of longitudinal location s:

$$x(s) = A\sqrt{\beta(s)}\cos(\psi(s)), \tag{2.63}$$

where A is the amplitude dependence on the initial conditions, $\sqrt{\beta(s)}$ describes the amplitude dependence on the machine lattice called Twiss parameter. Every particle has a different value of the amplitude of motion A, but this value stays constant everywhere in the machine lattice. $\beta(s)\cos(\psi(s))$ varies around the machine, but keeps the same for every particle in the beam. There are three Twiss parameters which describe the emittance ellipse (Fig. 2.10) – α, β and γ. The relations between them are the following:

$$\alpha(s) = -\frac{1}{2}\frac{\mathrm{d}\beta(s)}{\mathrm{d}s}, \tag{2.64}$$

$$\gamma(s) = \frac{(1+\alpha(s))^2}{\beta(s)}. \tag{2.65}$$

A random Gaussian distribution of particles forms a straight ellipse, which can be transformed into a circle if we chose the proper coordinates. The emittance ellipse is expressed by the equation:

$$\gamma x^2 + 2\alpha x x' + \beta x'^2 = A^2, \tag{2.66}$$

which obviously corresponds to (2.61).

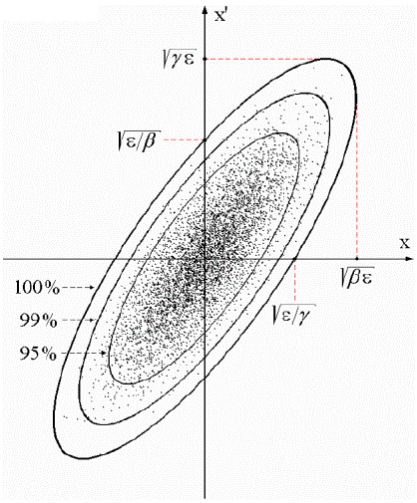

Figure 2.10: Emittance ellipse; ε – emittance, β, γ – Twiss parameters, $\sigma_x = \sqrt{\varepsilon\beta}$ and $\sigma'_x = \sqrt{\varepsilon\gamma}$ (2.77) ; [4]

2.4.2 Statistical definition of emittance

Often it is more practical to derive an emittance expression according to the distribution of particles in the phase space. The reason is simple: firstly, we usually get the angle and both positions from the beam measurement and secondly, the simulations become simplier. In the derivation of emittance equations we will mainly follow the article [1].
The coordinates of the 2D phase space are w for the position and w' for the angle. If we chose coordinate axis w and w', then the origin is situated in the barycentre. Consequently the expected values $\langle w \rangle$ and $\langle w' \rangle$ are zero. Moreover the second order moments of distribution in w-w' plane for total range of N particles are given by the relations:

$$\sigma_w = \sqrt{\frac{1}{N}\sum_{i=1}^{N} w_i^2}, \qquad \sigma_{w'} = \sqrt{\frac{1}{N}\sum_{i=1}^{N} (w'_i)^2}. \tag{2.67}$$

The area of the emittance can be written as characteristic width in the w axis multiplied by the characteristic width in the w' axis:

$$\varepsilon = \sigma_w \sigma_{w'}. \tag{2.68}$$

The expected values $\langle w \rangle$ and $\langle w' \rangle$ are not zero in the case that the distribution is rotated so a correlation between the position and the angle exists.
The measured (or simulated) coordinates of particles are denoted as x and x' and the original w, w' axes form an angle θ with x, x' axes, as depicted in Fig. 2.11.
From Fig. 2.11 we can write the relations for d_i (w coordinate of i^{th} particle) and d'_i (w' coordinate of i^{th} particle):

$$d'_i = |x'_i \cos\theta - x_i \sin\theta| = \sqrt{(x'_i \cos\theta - x_i \sin\theta)^2}, \tag{2.69}$$

$$d_i = |x'_i \sin\theta + x_i \cos\theta| = \sqrt{(x'_i \sin\theta + x_i \cos\theta)^2}. \tag{2.70}$$

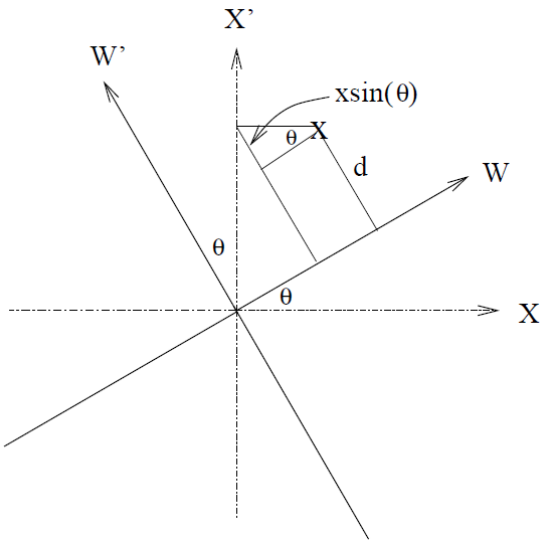

Figure 2.11: Rotation of phase space axes by angle θ, [1]

In [1], by using (2.69) and (2.70), the equations for $(\sigma_{w'})^2$ and $(\sigma_w)^2$ are derived. Here we only mention the following relations:

$$\sigma_{w'}^2 = \frac{1}{N}\sum_{i=1}^{N}(d_i')^2 = \frac{1}{2}\left(\langle x^2\rangle + \langle (x')^2\rangle - \sqrt{(\langle x^2\rangle - \langle (x')^2\rangle)^2 + (2\langle xx'\rangle)^2}\right), \tag{2.71}$$

$$\sigma_{w}^2 = \frac{1}{N}\sum_{i=1}^{N}(d_i)^2 = \frac{1}{2}\left(\langle x^2\rangle + \langle (x')^2\rangle + \sqrt{(\langle x^2\rangle - \langle (x')^2\rangle)^2 + (2\langle xx'\rangle)^2}\right). \tag{2.72}$$

Then emittance (also called *RMS emittance* discussed in 2.4.2):

$$\varepsilon = \sqrt{\sigma_w^2\sigma_{w'}^2} = \sqrt{\langle x^2\rangle\langle (x')^2\rangle - \langle xx'\rangle^2}, \tag{2.73}$$

where

$$\sigma_x^2 = \langle x^2\rangle = \frac{1}{N}\sum_{i=1}^{N}(x_i - \langle x\rangle)^2, \tag{2.74}$$

$$\sigma_{x'}^2 = \langle (x')^2\rangle = \frac{1}{N}\sum_{i=1}^{N}(x_i' - \langle x'\rangle)^2, \tag{2.75}$$

$$\sigma_x\sigma_{x'} = \langle xx'\rangle = \frac{1}{N}\sum_{i=1}^{N}(x_i - \langle x\rangle)(x_i' - \langle x'\rangle). \tag{2.76}$$

There is also a possibility to write the previous equations for emittance via determinant. This method is very effective for 6D phase space, as reported in [1].
The statistically measurable parameters σ_x and σ_x' can be rewritten by the emittance ε and Twiss parameters α, β and γ:

$$\sigma_x = \sqrt{\varepsilon\beta}, \qquad \sigma_x' = \sqrt{\varepsilon\gamma}, \qquad r\sigma_x\sigma_x' = -\alpha\varepsilon, \tag{2.77}$$

where r is the radius of a circle in the phase space [1].

Normalized emittance

Normalized emittance ε' can be described by the relation:

$$\varepsilon' = \beta\gamma\varepsilon, \tag{2.78}$$

where β and γ are relativistic parameters and ε is the not-normalized emittance.
We introduce this term, because it is often very useful to consider the normalized emittance than the not-normalized one due to a so-called adiabatic damping. The basis of this effect is that emittance is inversely proportional to beam momentum [32], which, finally, reduces the physical size of the beam. Thus one of the greatest advantages of the normalized emittance consist in not changing with the energy, so the beam degradation can be observed.

Root mean square (RMS) emittance

When we consider not only a single particle but a distribution of them, it is useful to use the root mean square emittance. From a statistical point of view, the RMS emittance is defined as the root mean square [39] of this quantity and is described via (2.73). It is usually used for a Gaussian beam. In addition the term is also needed in real measurements of beam emittance. In fact, it is hard to get the full width of the beam, but it is easier to measure the RMS width [32].

Chapter 3

Setting up a program for ion beam transport in magnetic solenoid

3.1 The main idea of the program

The main goal of my work was to write a matlab program which can compute the trajectory coordinates of a charged particle beam in a solenoid with given starting conditions for the position and the velocity coordinates r_0, θ_0, z_0 and $v_{r_0}, v_{\theta_0}, v_{z_0}$. The charged particle motion through the solenoidal field is written in a cylindrical coordinate system. A transformation into Cartesian coordinates is used only for plotting. The solution (by numerical mode, using matlab subroutines) of a system of differential equations which we will discuss in chapter 3.2, along to obtain the coordinates of movement moreover a file for generating the particle beam emittance is also generated. By changing parameters we can study the behaviour of charged particles (or a single particle) in the solenoidal field – for example a fringing field effect.

3.2 The program itself, explanation of the matlab code

In this section we will explain the codes one by one referring to the knowledge that we have already discussed, especially in part of the second chapter 2 *(Behaviour of charged particle beams in a solenoid magnetic field)*. The matlab syntax is taken from [6]. All the sub-programs, functions and plotting files are located in Appendix 4.3.2 with brief comments.
In the whole code we will use y as a vector with the following cylindrical components: $y = (r, v_r, \theta, v_\theta, z, v_z)$.

3.2.1 Main code

The first part of the *main code* consists of setting parameters and constants. Firstly, I have set wire current i [A], number of wire turns N [-], the solenoid's position on z axis: $zini$ [m] means position of the left end of the solenoid and $zfin$ [m] of the right end of the solenoid, so the length of the solenoid l can be expressed as $l = zfin - zini$ [m], r [m] is radius of the solenoid and b_0 is the original magnetic field in the solenoid centre (along z-axis) computed due to the relation (2.22) and just for clarity – the number $1.26E$-6, used in the relation for b_0, is the value of permeability vacuum in Hm^{-1}. Finally, *clf* command on the top is

only for getting our start "clean", because it clears the current figure window.

```
clf
time=cputime;
i = 1800;
N = 1200;
zini = 0.1;
zfin = 0.25;
r = 0.025;
bo=(1.26E-6*i*N)/sqrt((zfin-zini)^2+4*r^2)
```

The following part sets the beam parameters – kinetic *energy* [eV], proton rest energy E_0 [eV], relativistic factors γ, β and *velmod* – total velocity of the charged particle (or of the beam in the case of more particles). The relation $\gamma = 1 + energy/E_0$ is a simple adaptation of the total energy E:

$$E = E_0 + E_k, \tag{3.1}$$

$$mc^2 = m_0c^2 + E_k, \tag{3.2}$$

$$E_0\gamma = E_0 + E_k, \tag{3.3}$$

$$\gamma = 1 + \frac{E_k}{E_0}, \tag{3.4}$$

where kinetic energy $E_k \equiv energy$ in the matlab code.

```
energy= 30e6;
Eo=938e6;
gamma=1+energy/Eo;
beta=sqrt(1-1/gamma^2);
velmod=beta*(2.998e+8);
```

The program continues with time setting of ordinary differential equations. From maximum length of total path L_{tot} we will get the final time for the particle motion t_{max0} [s]. Naturally, we are starting from $t_{min0} = 0$ s. In addition, time points which define the integration interval of ODEs are specified by *tspan0* vector. The integration starts in t_{min0} and ends in t_{max0} and the solution is evaluated in $t_{max}/1000$ steps.

```
Ltot=1;
tmin0=0;
tmax0=Ltot/velmod;
tspan0=[tmin0:tmax0/1000:tmax0];
```

Now we have to transform the three-dimensional Cartesian coordinates stored in x, y and z to the cylindrical ones stored in r, θ, z. This is done by *cart2pol* matlab syntax. *Velr* is velocity

in radial direction and can be expressed as follows:

$$velr = \sqrt{v_x^2 + v_y^2}, \tag{3.5}$$

$$v_x = \frac{\mathrm{d}x}{\mathrm{d}t} = \frac{\mathrm{d}x}{\mathrm{d}s}\frac{\mathrm{d}s}{\mathrm{d}t} = x'velmod, \tag{3.6}$$

$$v_y = \frac{\mathrm{d}y}{\mathrm{d}t} = \frac{\mathrm{d}y}{\mathrm{d}s}\frac{\mathrm{d}s}{\mathrm{d}t} = y'velmod, \tag{3.7}$$

$$velr = \sqrt{(x'velmod)^2 + (y'velmod)^2}, \tag{3.8}$$

where s is the longitudinal direction and x', y' are divergences in x, y directions. Another nedeed step is to set the right units. The output from *beam emittance* file 3.2.3 has a certain unit, which depends on the value that is set from the emittance *eps0* – in this case $[\pi \cdot mm \cdot mrad]$. Therefore the dividing factor 1/1000 is necassary to obtain position *posx* in [m] and divergence *pospx* in [rad]. So it can look like this:

```
[ttheta,rr,zz]=cart2pol(posx(:,1)/1000,posx(:,2)/1000,0);
r0=[rr,ttheta];
velr=sqrt((posxp(:,1)*velmod/1000).^2+(posxp(:,2)*velmod/1000).^2);
k=1;
```

If we want a more realistic approach, it is better to set the dividing factors of *pospx* to 1/100 (hundreds mrad) and of *posx* to 1/10000 (*posx*) because of the laser spot size. Generally the spot diameter which the laser generates by the interaction is 50 microns or more. For now, for clarity, we take the factor of 1/1000. This "unit setting" can also be done by changing the Twiss parameters which, however, means running again the *beam emittance* file 3.2.3, so using the dividing factors seem to be a better solution.
Then, the program solves the differential equations from 3.2.2 with the initial vector y_0 (with its coordinates $y_0 = (r_0, v_{r_0}, \theta_0, v_{\theta_0}, z, v_{z_0})$, which consists of six elements – three initial conditions for position and three for velocity. As we can see in the code $v_{\theta_0} = 0$ (straight trajectory), $z = 0$ (we start from zero point, it is just a question of choice of coordinate system) and v_z can be expressed as $v_z = \sqrt{v^2 - v_r^2}$, where v is total velocity *velmod*. Moreover there is a possibility to introduce the starting conditions by a data file. The line *row=1:1:Np* means that we are solving ODEs for each of N_p particles *Reltol* (relative tolerance) was used as an error control property. This error must be less than or equal to the acceptable error 10^{-7}. We have to set the *Reltol*, because the accuracy of our result is influenced by the tolerances, which are used for limiting the local discretization error. When the difference between the high-accuracy and the low-accuracy step is higher than our tolerance, the step size is reduced. Of course, each tolerance must fit in its own program, because setting a too low or a too high tolerance is not good. In order to solve the function of ODEs I used *ode45* (which originally has value of *Reltot* 10^{-3}) and the needed subprogram with differential equations reported in 3.2.2. The *odeset* function adjusts various parameters, which we have already discussed. The information from ODEs solving is saved in *cylcoord* for each (k-th) particle. Because of this we have to set a counter of particle number from k to $k + 1$ in the *for loop*.

```
for row=1:1:Np;
y0=[r0(row,1),velr(row),r0(row,2),0,0,sqrt(velmod^2-velr(row)^2)];
options=odeset('reltol',1e-7);
[t0,y]=ode45('solutionODEcylind3D',tspan0,y0,options,i,N,zini,zfin,r);
```

```
cylcoord(:,:,k)=y;
k=k+1;
end
```

The following part is only a simple transformation of all the information from cylindrical coordinate system to the Cartesian one, because of the matlab plot which expects Cartesian coordinates. This is done in three steps: firstly, *cylcoord*s are transformed to Cartesian xx, yy, zz; then this transformation is done for each particle and finally, all three coordinates are saved into new Cartesian *coord*.

```
for kk=1:1:(k-1)
[xx,yy,zz]=pol2cart(cylcoord(:,3,kk),cylcoord(:,1,kk),cylcoord(:,5,kk));
end
for kk=1:1:(k-1)
[xx(:,kk),yy(:,kk),zz(:,kk)]=pol2cart(cylcoord(:,3,kk),cylcoord(:,1,kk),
cylcoord(:,5,kk));
end
for kk=1:1:(k-1)
coord(:,:,kk)=[xx(:,kk),yy(:,kk),zz(:,kk)];
end
```

The last part of the *main code* plots the trajectories of charged particle beam in z-y, z-x and y-x plane. The simple 3D graph is also included and total computing time is evaluated.

```
or k=1:1:Np
hold on
subplot(2,2,1);
plot(coord(:,3,k),coord(:,2,k)); %zy plane
hold off
hold on
subplot(2,2,2);
plot(coord(:,3,k),coord(:,1,k)); %zx plane
hold off
hold on
subplot(2,2,3);
plot(coord(:,2,k),coord(:,1,k)); %yx plane
hold off
hold on
subplot(2,2,4);
plot3(coord(:,3,k),coord(:,2,k),coord(:,1,k)); % 3D
hold off
end
e=cputime-time
```

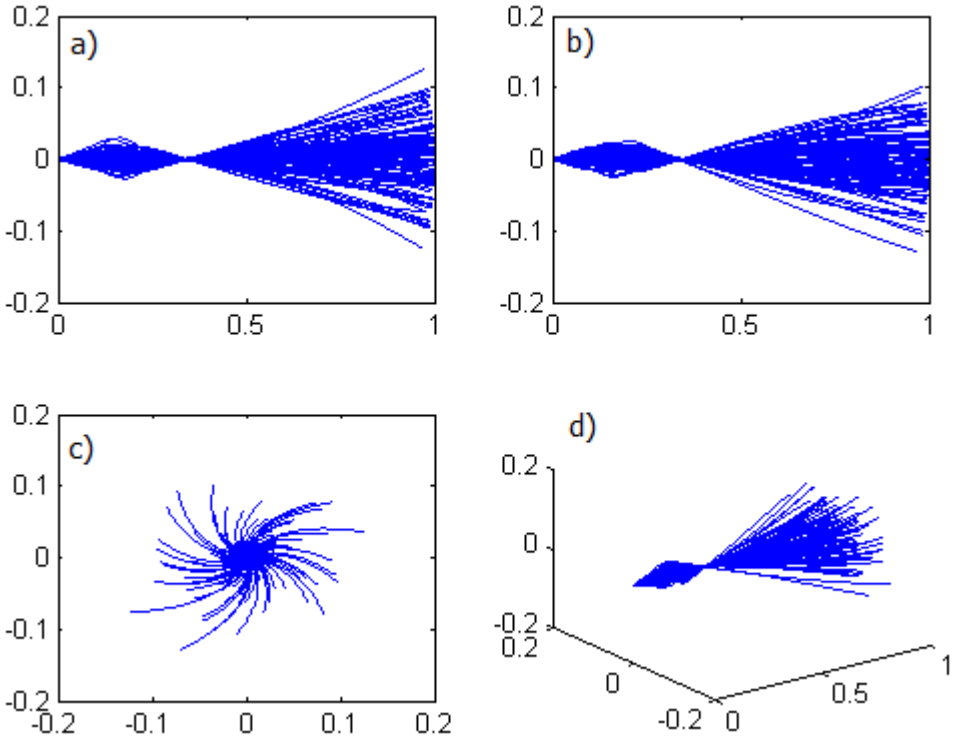

Figure 3.1: Spatial views of a charged particle beam trajectory; a) z-y plane, b) z-x plane, c) y-x plane, d) $3D$ graph; $bo = 17,21293$ T; $e = 12,3085$ s

3.2.2 Solution of cylindrical ODEs

For solving differential equations of motion in solenoidal magnetic field the *main code* 3.2.1 uses the following sub-program. For better clarity we will separate it into three parts where the cylindrical coordinates are used.
The first part sets parameters – atomic mass unit *amu* [kg], elementary charge e [C], mass number of proton A_p, charge state Q, permeability constant *mu_ 0* [H/m], length of solenoid L [m] (where *zfin* is position of the right end of the solenoid on z-axis and *zini* is the left one), $z1$ and $z2$ are distances, on the axis, from the ends of the solenoid to the magnetic field measurement point = position of the particle, as it is shown on Fig. 2.4. Mass number of proton is the mass of proton divided by $1u$, where u is the atomic mass unit.

```
function [dydt]=f(t,y,nothing,i,N,zini,zfin,r)
amu=1.66053886e-27;
charge = 1.60217653e-19;
Ap=1.00727647;
Q = 1;
mu_0=1.26E-6;
L = (zfin - zini);
z2 = y(5) - zini;
z1 = y(5) - zfin;
```

Secondly, the elements of the magnetic field are computed. For evaluating B_z we use the relation (2.20), $B_\theta = 0$ because there is no angle-dependence (see chapter 2.3.2) and B_r is computed due to the relation (2.54). The simple derivation of the radial component of the magnetic field is shown here:

$$B_r = -\frac{r}{2}\frac{\partial B_z}{\partial z}, \qquad B_z = \frac{\mu_0 IN}{2L}\left(\frac{z_2}{\sqrt{z_2^2+r^2}} - \frac{z_1}{\sqrt{z_1^2+r^2}}\right) \tag{3.9}$$

$$B_r = -\frac{r}{2}\frac{\mu_0 IN}{2L}\left(\frac{1}{\sqrt{z_2^2+r^2}} - \frac{z_2^2}{\sqrt{z_2^2+r^2}} - \frac{1}{\sqrt{z_1^2+r^2}} + \frac{z_1^2}{\sqrt{z_1^2+r^2}}\right) \tag{3.10}$$

```
bz=(mu_0*i*N)/(2*L)*(z2/sqrt(z2*z2+r*r)-z1/sqrt(z1*z1+r*r));
btheta=0;
br=-0.5*y(1)*(mu_0*i*N)/(2*L)*(1/sqrt(z2*z2+r*r)-1/sqrt(z1*z1+r*r)
-z2*z2/(z2*z2+r*r)^(1.5)+z1*z1/(z1*z1+r*r)^(1.5));
```

Finally, the 3 differential equations for focusing (2.58), rotation (2.59) and acceleration (2.60) are following in the syntax of solving function [6]. For clarity I have also defined the *ratio_ QA*:

$$ratio\_QA = \frac{Q}{A_p}\frac{e}{u} = Q\frac{u}{m_p}\frac{e}{u} = \frac{eQ}{m_p}, \tag{3.11}$$

where, as we have already mentioned, Q is charge state, e is elementary charge, A_p is mass number of proton, u atomic mass constant and m_p mass of proton. It is also possible to set general A and general ratio $ratio\_QA_{gen} = eQ/(uA)$ and in the case $A = 1$ (proton) the relation $ratio\_QA = ratio\_QA_{gen}$ is valid. This allows us to consider a wide range of particles.

```
ratio_QA=Q/Ap*charge/amu;
   dydt=[y(2)
         ratio_QA*y(1)*y(4)*bz+y(1)*y(4)^2
       y(4)
         (ratio_QA*(y(6)*br-y(2)*bz)-2*y(2)*y(4))/y(1)
       y(6)
         -ratio_QA*y(1)*y(4)*br];
```

3.2.3 Beam emittance

The program generates the starting conditions (x, x' and y, y') of particles with *initial* emittance *eps0*. The output files are *posx* (where coordinates are stored) and *posxp* (where divergences are stored). By *plot emittance* file 3.2.5 we can see in the phase space the x-x' and y-y' emittances of particles. We have already discussed the theory which we will need in matlab sub-program computing emittance in chapter 2.11.
Again we will start with cleaning our working environment (*clear all*) and setting the variable for computing time. Then, the parameters are set – Twiss parameters α, β, γ (chapter 2.4.1), initial RMS emittance [π mm rad] (chapter 2.4.2), number of particles N_p and the statistically measurable parameters (in terms of Twiss parameters and emittance) *xrms*=σ_x [mm] (defined by relation (2.74)) and *xprms*=$\sigma_{x'}$ [mrad] (defined by relation (2.75)).
We have to pay attention to the designation of Twiss parameters, because two of three Greek letters have already been used for the relativistic factors. The Twiss parameters γ and α are set as constants and the parameter β satisfies the relation (2.65).

```
clear all;
time=cputime;
gamma=15
alpha=-2
beta=(1+alpha^2)/gamma
eps0=5.;
Np=100;
xrms=sqrt(eps0*beta)
xprms=sqrt(eps0*gamma)
```

The following lines are used for allocating memory array for x, y and x', y' planes. The *count* is a counter which is needed for the later while-cycle. The syntax *zeros(Np,2)* returns an Np-by-2 array of zeros where the number of particles N_p naturally indicates the variable dimension. *Posx* is a storage for coordinates of particles and *posxp* for divergences.

```
count=0;
posx=zeros(Np,2);
posxp=zeros(Np,2);
emittance=zeros(Np,2);
```

The main while-cycle of the *beam emittance* file is repeating until the *posx*, *posxp* and *emittance* will not be computed for all the particles (N_p). Firstly, the random 1-by-2 array x with Gaussian distribution ($\sigma_x = xrms(x, y)$, μ=0) and random 1-by-2 array xp also with Gaussian distribution ($\sigma_{x'} = xprms(x', y')$ and μ=0) are generated. The emittance *eps* on x-y plane is computed on the basis of relation (2.66).
As we see in the code it is required that the initial emittance *eps0* is 9 times larger than emittance *eps* and *xrms* is 3 times larger than $\sqrt{x^2(1,1) + x^2(1,2)}$ which is the length of the vector connecting the particles position in the phase space with the centre of the emittance ellipse (Fig. 2.10). Why 9 or 3 times? Because the particles are distributed in a phase space which is 3 times the size (*xrms*) we set. That allows to take into account of the beam halo of the hypothetical normal distribution of the real beam. Since the emittance is proportional to the square of the size of the beam (2.68), the real emittance also must be 9 times *eps0*.
For each particle of the total N_p particles, in *posx* the coordinates of the particles are stored (x-y plane), in *posxp* the divergences are stored (x'-y' plane) and in the *emittance* the emittance *eps* is located.
With help of counter *count* we can include all the particles in a while-cycle. Finally, the picture of the situation in x-x' plane is generated and the time needed for the *beam emittance* sub-program is evaluated.

```
while count<Np
    x=normrnd(0,xrms,1,2);
    xp=normrnd(0,xprms,1,2);
    eps= gamma*x.^2+2*alpha*x.*xp+beta*xp.^2;
       if eps<9*eps0 & sqrt(x(1,1)^2+x(1,2)^2)<3*xrms;
        count=count+1;
        posx(count,:)=x;
        posxp(count,:)=xp;
        emittance(count,:)=eps;
```

```
        end
end
plot(posx(:,1),posxp(:,1),'.');
axis equal;
e_time=cputime-time
```

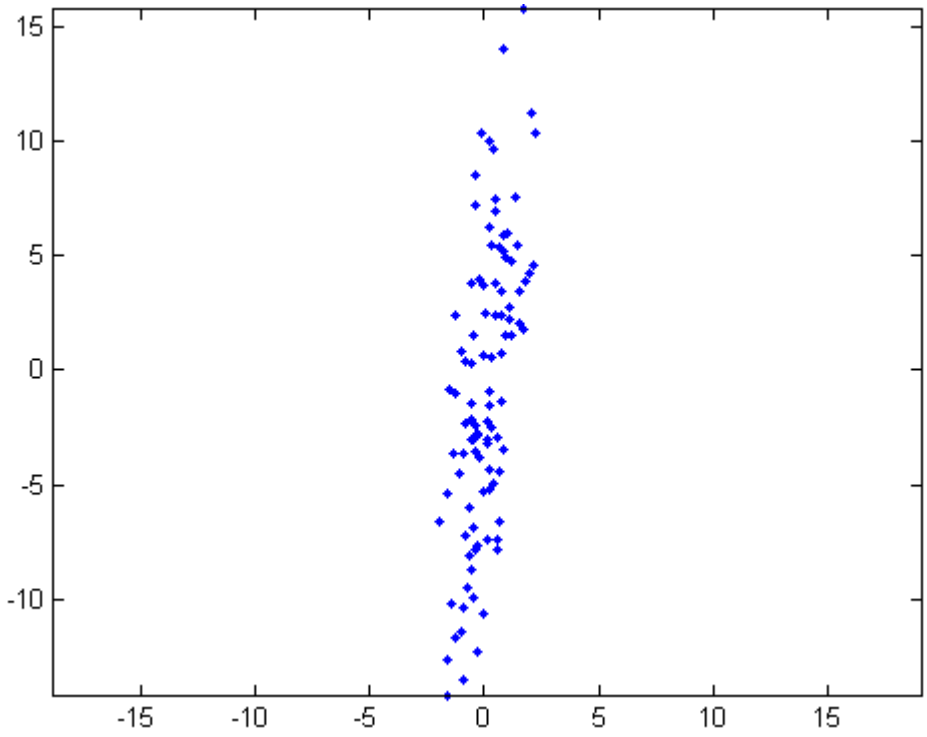

Figure 3.2: Plotted emittance in x-x' plane with parameters $\gamma = 15$ rad/m; $\alpha = -2[-]$; $\beta = 0,3333$ m/rad; $xrms = 1,2910$ mm; $xprms = 8,6603$ mrad; $e\_time = 0,1560$ s

3.2.4 Energy calculation

The program allows us calculating kinetic energy from velocity for each of the N_p particles. The kinetic energy is computed on the basis of equation (3.4). Moreover, the velocity for each particle is computed with consideration to the equation:

$$v = \sqrt{v_x^2 + v_y^2 + v_z^2}. \tag{3.12}$$

For completeness, the well-known relations for relativistic parameters γ and β are used:

$$\beta = \frac{v}{c}, \tag{3.13}$$

$$\gamma = \frac{1}{\sqrt{1-\beta^2}}, \tag{3.14}$$

where c is speed of light, numerically $c = 2,9998 \cdot 10^8$ m·s^{-1}.

```
clear velocity;
kkk=1
for kk=1:1:Np
velocity(:,:,kk)=sqrt(coord(kkk,2,kk)^2+coord(kkk,4,kk)^2+coord(kkk,6,kk)^2);
kkk=kkk+1;
end
beta1=velocity/(2.9998e+8);
gamma1=1/sqrt(1-beta1.^2);
Ekin1=(gamma1-1)*Eo;
```

3.2.5 Plotting emittances

The *plot emittance* file id depicted by dots the x-x' and y-y' emittance of all particles in the phase space.

```
subplot(2,1,1);
plot(posx(:,1),posxp(:,1),'.');
axis square;
subplot(2,1,2);
plot(posx(:,2),posxp(:,2),'.');
axis square;
```

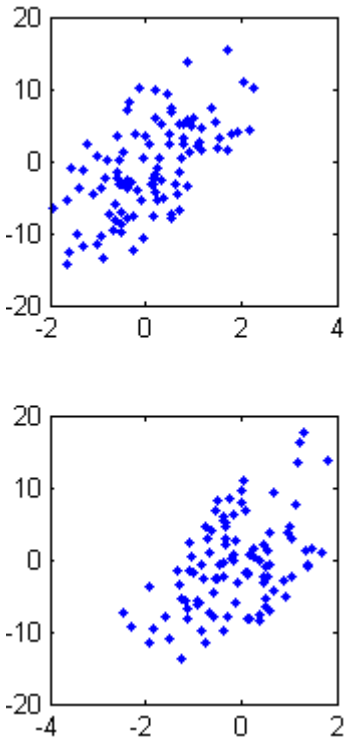

Figure 3.3: Plotted emittances in x-x' and y-y' plane with parameters $\gamma = 15$ rad/m; $\alpha = -2[-]$; $\beta = 0,3333$ m/rad; $xrms = 1,2910$ mm; $xprms = 8,6603$ mrad; $e\_time = 0,1560$ s

3.3 Fringing field effect

The fringing field is the magnetic field region surrounding a magnet and depends on the type of this magnet (solenoidal) and field strength, meaning that higher field strength corresponds to a larger fringe field.
Generally in the first order, in particle beam optic it is used to neglect the effect of the stray field on the dynamic calculation: this model is called the "hard edge". In reality, however, since nature does not allow sudden changes of physical quantities the hard edge model is only an approximation, although for practical purposes a rather good one. In a real magnet the field strength does not change suddenly from zero to full value but rather follows a smooth transition from zero to the maximum field. Sometimes, the effects due to this smooth transition or fringe field are important and we will derive the appropriate corrections in this section.
If we change the radial field to zero value ($B_r = 0$ T), then we get a uniform field where the fringing field is absent. Now, if we compare Fig. 3.1 with Fig. 3.4 or more precisely their third pictures with changes in beam trajectories projection (in x-y plane), we can see that the charged particles in the first graph move on "circular" trajectories (we are still speaking projection of trajectories) with cyclotron frequency (2.3) which causes focusing (see Fig. 2.6). We will try to explain why the trajectory projection of charged particle beam with $B_r = 0$ has straight lines as it is shown in the third graph on Fig. 3.4. The components of the solenoid magnetic field derived in chapter 2.3.2 are described by relations (2.54) and (2.55). Then for z-coordinate of the magnetic field we obtain:

$$B_r = -\frac{1}{2} r \frac{\partial B_z}{\partial z}, \tag{3.15}$$

$$B_z = -\frac{2B_r}{r} \int \mathrm{d}z = -\frac{2B_r}{r} z. \tag{3.16}$$

When we use result (3.16) and substitute it into (2.2) and do the limit for $B_r \to 0$, then, for the trajectory radius r it can be written:

$$r = \frac{P_\perp}{eB_z} = \frac{P_\perp r}{-2eB_r z}, \tag{3.17}$$

$$\lim_{B_r \to 0} r = \lim_{B_r \to 0} \frac{P_\perp r}{-2eB_r z} = \infty. \tag{3.18}$$

Since we can imagine a straight line like a circle with an infinite radius, this is the connection and explanation of the differences between c) graphs on Fig. 3.1 and Fig. 3.4. The comparison between the other three graphs is very hard to be seen – they look very similar, because the main difference between fringing and non-fringing field is the increment in velocity v_θ. From the chapter 2.2 we know that the increment in azimuthal velocity on boundary between 1^{st} and 2^{nd} region (same notation) is given by the relation (2.28): $\Delta v_\theta = r_0 \omega_L$, respectively (2.33) for boundary between 2^{nd} and 3^{rd} region. The increment with consideration of non-fringing field will be derived in a simple way. We use relations (2.54) and (2.5):

$$B_r = \frac{-1}{2} r \frac{\partial B_z}{\partial z} \qquad \Leftrightarrow \qquad B_z = \frac{-2B_r}{r} z, \tag{3.19}$$

$$\omega_L = \frac{eB_0}{2\gamma m} = 0, \tag{3.20}$$

$$\Delta v_\theta = r_0 \omega_L = 0. \tag{3.21}$$

Thus the increment in azimuthal velocity v_θ is zero in the case of the non-fringing field and non zero in the case of the fringing field.

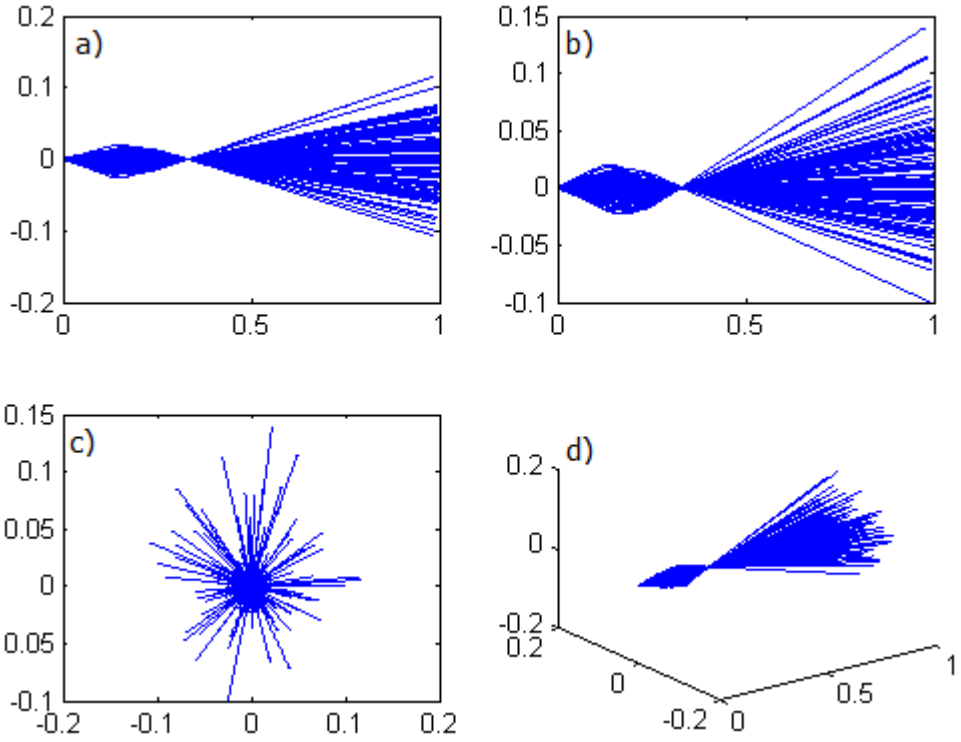

Figure 3.4: Spatial views of a charged particle beam trajectory with a non-fringing field ($B_r = 0$ T); a) z-y plane, b) z-x plane, c) y-x plane, d) $3D$ graph; $bo = 17,21293$ T; $e = 12,3085$ s

Chapter 4

Application of laser-accelerated protons in hadrontherapy

4.1 Hadrontherapy

One of the applications of accelerated ion beams with great impact on society is hadrontherapy. Hadrontherapy is a radiological technique which deals with treatment of cancerous tumours by using strongly interacting particles – protons (better dose distributions), neutrons (better tumour killing), pions or ions (α, C, Ne) [10].

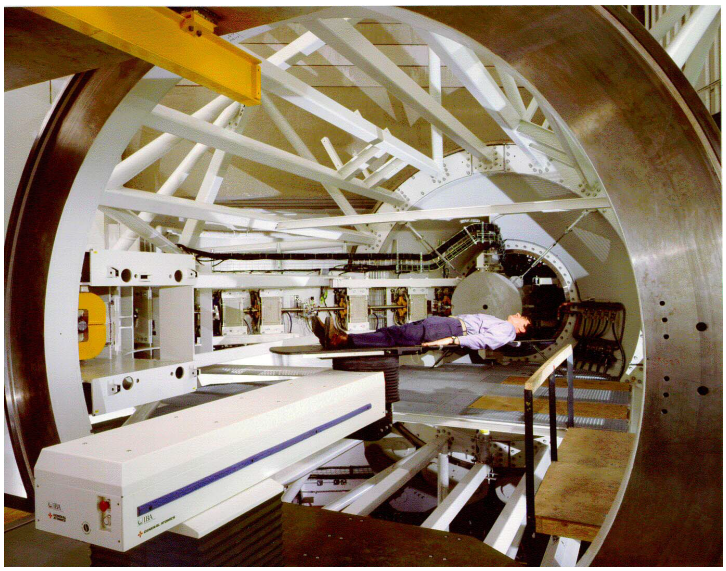

Figure 4.1: A gantry in the Northeast Proton Therapy Center, [21]

Although several hadron therapy facilities based on conventional acceleration machines are operational worldwide, laser-driven hadron therapy centers are still not present since they do not fit within the strict radiological requirements (energy, dose ...) yet. On the other hand several projects are active worldwide based on the idea of treating cancer by laser driven ion beams. In fact these methods can potentially drastically reduce the size and as a consequence the cost of future hadron therapy centers. Studies on the biological effect of laser-driven ions

on living cells are already abundantly performed. In fact it is crucial to better understand the biological consequence of short ion bunches associated with the ultra short laser beams.

4.1.1 Physical rationale

The enormous advantage of using protons or ions for cancer treatment is their energy deposition property. In contrast with X-rays (photons), protons show an increasing energy deposition with the increase of the penetration distance. The energy deposition for some time remains steady and, near the end of the particle trajectory, is followed by a sharp increase leading to the maximum of energy deposit – the Bragg peak. This dependence is shown in Fig. 4.2 a).

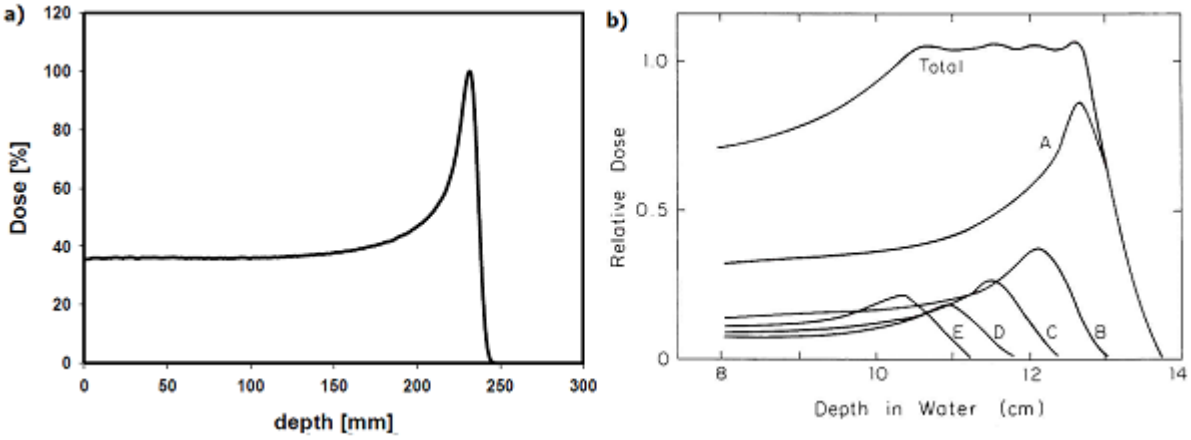

Figure 4.2: a) Dependence of typical dose deposition on penetration depth for a proton beam; [21], b) a proton beam can be precisely shaped (in three dimensions) to fit to the area of tumour. Making the area of maximum relative dose in required depth wider consists of putting together more energy deposition curves with different space-position of their Bragg peak; [10].

This characteristic allows minimization of the effect on the surrounding healthy tissue, while only the tumour is being treated. In fact, protons are losing their energy in atomic or nuclear interactions and they slow down faster than photons, because of their non-zero mass. The comparison between proton therapy and photon therapy is reported in chapter 4.1.2. The decreasing energy of protons avoids greater interactions with orbit electrons which, finally, causes the increasing energy. Obviously the maximum interaction with electrons appears at the end of the range noted as Bragg peak. In other words, the protons deposit more energy when they are slowing down and this energy is culminated in the Bragg peak [28]. A possibility as to how to cover the whole tumour volume is presented in the Fig. 4.2 b). Proton beam can be precisely shaped in three dimensions to fit to the area of tumour. The idea consists of putting together more energy deposition curves with different space-possition of their Bragg peak to create this peak much wider.

4.1.2 Clinical rationale

Proton therapy can be used for irradiating tumours which are located close to places where a small local overdose can cause fatal complications. This includes tumours close to the spinal cord, paediatric optic, esophageal cancer, prostate cancer etc.

Proton therapy has already been applied for the treatment of paranasal sinus tumours, chordoma, chondrosarcoma, meningioma, prostate and lung tumours [21] (data from year 2005). The typical proton energy range for clinical interest is $60-250$ MeV, depending on the location of the tumour. The typical dose for one treatment is $1-5$ Gy (one Gy=gray is the absorption of one joule of energy per kilogram [36]) with typical currents 10 nA and $1,2$ nA for protons and carbon ions. The biggest advantage of carbon ions is their higher biological effectiveness, thus they are used mainly for treating radio resistant and hypoxic tumours. On the other hand, magnetic steering systems (=gantries) are huge and heavy – for carbon ions they can weight approximately 500 tons, but proton gantries weigh "only" 100 tons. Laser-driven accelerators (chapter 4.2.1) could be a solution since they can avoid the use of gantries. The limitation is the fact that proton energy obtained from a laser accelerator is quite low, so potentially they can treat only patients with tumours a few centimetres under the skin – eye tumours, thyroid, larynx, nasal or paranasal cavity, breast, superficial lymph node, skin and subcutaneous tissue [19].
A summary of the obtained results with hadrontherapy is reported in Tab. 4.3 situated in Appendix 4.3.2.

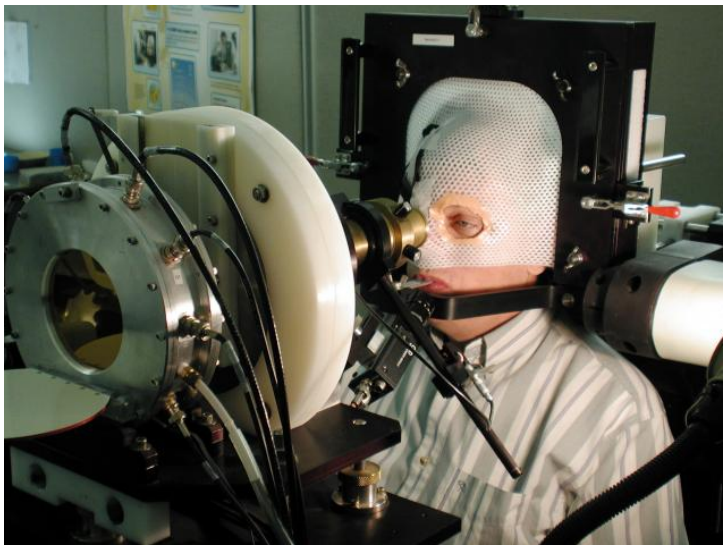

Figure 4.3: Proton therapy for an eye tumour – the treatment of choice for choroidal melanomas; [3]

Why prioritize proton therapy before X-ray radiation?

The crucial problem with using X-rays for treatment is their problematic controlling as an energy source. Most body tissue cannot absorb and stop X-rays, so they pass through and irradiate not only the treated tumour but also the healthy tissue. The tissue damage as a result of X-rays can cause serious health problems, especially when the sensitive or life-crucial areas like brain, lungs (Fig. 4.4) or eyes are treated [9].
On the other hand, proton therapy has no "exit dose" of radiation like X-ray therapy has. A proton beam releases increasing energy when it starts to slow down, and the most energy (the Bragg peak) when it stops. After that there is a very little amount of residual energy. A small dose, compared to another treating methods, causes better retention of organ functions

and decreases the likelihood of secondary tumors in the future [24].

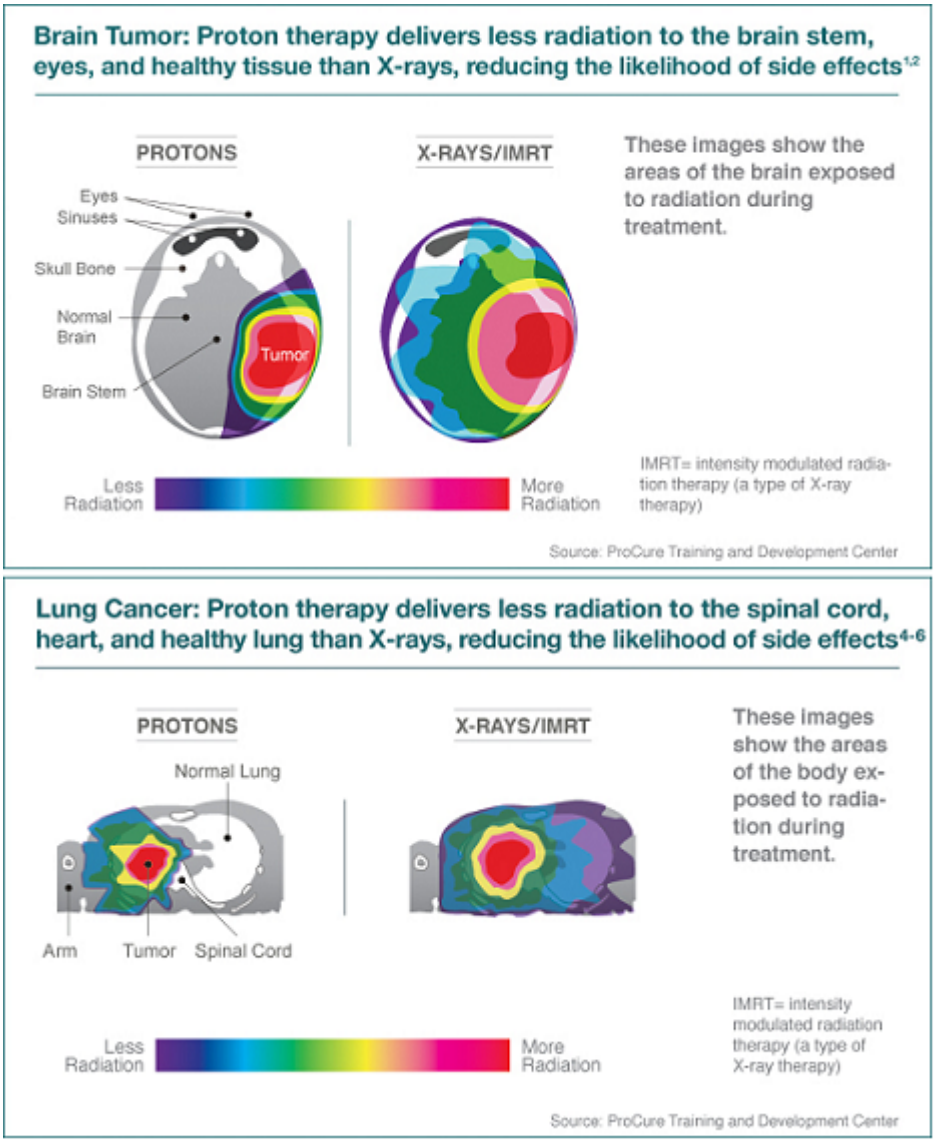

Figure 4.4: Differences of radiation amount between protons and X-rays/Intensity-Modulated Radiation Therapy illustrated on examples of brain and lung tumour; [24]

4.2 Classic proton accelerators and their comparison with laser accelerators

In many cases the particle beams are accelerated by conventional accelerators like synchrotrons or cyclotrons. However, the laser acceleration of charged particles may be taken as an alternative technology for hadrontherapy. Moreover, there are also some undeniable advantages which we will discuss later. Sadly, they are followed by limitations in proton energy (several tens of MeVs), which we are able to reach at present.

Some experiments and simulations [19] show that, although the basic acceleration mechanisms are well described and known, the medical applications require new mechanism of acceleration.

4.2.1 Laser accelerators

The expectations from laser ion accelerators are to be compact, simple and low cost.
Due to the last thing on this list, it will also be more possible to set hadrontherapy based on laser acceleration to hospitals and make treatment more achievable. Furthermore, the gantries are small with no large magnets and radiation shielding is only local, so the acceleration mechanism can take place in a gantry or the patient's room, not in a distant place like conventional accelerators have to. Another advantage, as we have already mentioned, is the absence of huge magnets or ion injectors. Conventional accelerators need a large number of magnets because of the protons (e.g. 200 MeV), which have to be bent by 135 degrees. In contrast, laser accelerators have a much lower bending angle because protons are generated much closer to the patient. The trajectory of protons or ions is shaped by magnets and laser light redirected in transport by mirrors. The last mirror focuses the laser onto a target which is an accelerator itself of the size $0,1 - 1$m (Rear and Front surface acceleration 1.2) [19].
The irradiation multi-terawatt system of a laser ion accelerator contains a final laser pulse compressor, an ion beam generation chamber, a separation magnet system and a patient positioning system. Nowadays multi-terawatt lasers, which easily fit into a common hospital room, are available for practical usage. This makes a proton therapy device size-comparable with the X-ray linac machines in many typical hospitals. As we discuss in 4.1.2 the tissue surrounding tumour will be less irradiated by using hadrontherapy treatment than by the X-ray one. From a financial point of view, the most expensive part of a laser accelerator is the laser itself. However laser technology is developing very quickly and high power laser system will become cheaper.
From simulations we know [19] that to generate ions over 100 MeVs, the intensities of 10^{20-21} Wcm^{-2} are necessary, thus laser peak power higher than 100 TW on target will be needed (we consider focusing onto an area of 10^{-6} cm^2 or smaller). Usually, only a small fraction of the laser pulse energy has therapeutic relevance. In fact, experiments usually deliver approximately $1-10\%$ of laser pulse energy to protons [19]. Thus new acceleration geometries aimed at increasing the conversion efficiency of the laser energy into accelerated protons are being proposed [16].

4.2.2 Conventional accelerators

Conventional accelerators are based on radio-frequency. In this paper we consider two types of them – cyclotron and synchrotron.

Cyclotron

A cyclotron is a type of particle accelerator. A static magnetic field (magnetic component of the Lorentz force) acts on moving charged particles and bends their trajectory into a semicircular path between acceleration by an applied rapidly varying (radio frequency) electric field. This electric field accelerates the charged particles just at the time when they finish their half circle path. Thus, the acceleration happens in the gap between dees (D-shaped electrodes) [20]. After several times of repeating this process, the accelerated particles exit the port with very high velocity. A simplified schema of a cyclotron is shown in Fig. 4.5.

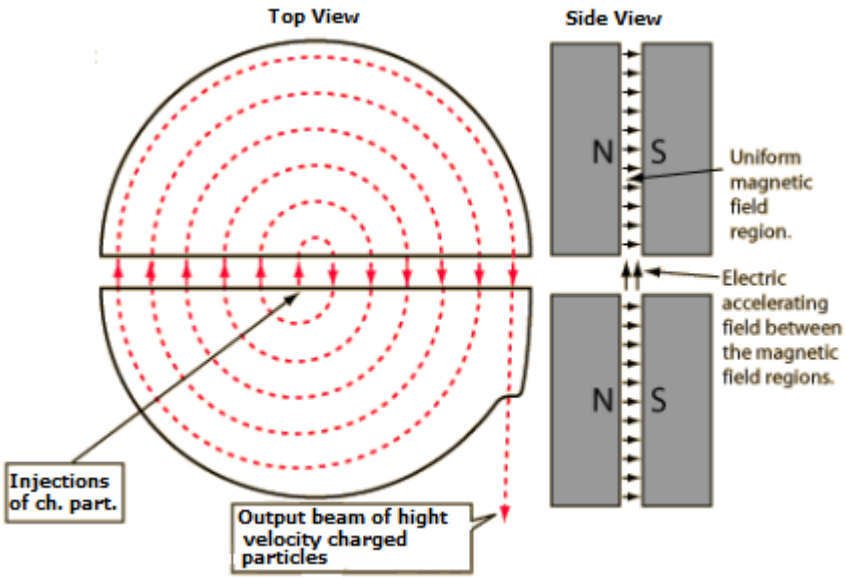

Figure 4.5: Cyclotron – particle accelerator; [20]

Synchrotron

A synchrotron is a type of particle accelerator, whose design is based on the concept of a cyclotron with the difference being that the magnetic field (which bends the trajectory of the particles) is time-dependent and synchronized to a particle beam of increasing kinetic energy. The synchrotron is good for constructing large facilities, because bending, beam focusing and acceleration can be separated into different components [40].

4.2.3 Requirements on accelerators and comparison between laser and conventional accelerators

There are four main requirements on accelerators [19] to achieve precise irradiation of irregularly shaped tumours:

- beam size control,
- intensity control,
- fast beam cut-off,
- time-structure control.

The comparison between conventional hadron therapy centers and potential laser-driven hadron therapy facilities is reported in Tab. 4.1:

Parameter	Conventional accelerators (synchrotron, cyclotron)	Laser driven accelerators
Beam transport	– large magnetic system required to bend charged particles – radiation shielding required around the bending corner	– laser beam can be transported and bended by mirrors (small device) – radiation shielding not required around the bending corner
Beam size	~ 10 mm	< 1 mm (at source)
Accelerator	– large magnetic system required to accelerate charged particles – total system is large and overall radiation shielding required	– only target part should be irradiated – compactification of the system possible
Irradiation system	– three to five meter magnetic system required to bend charged particles $90 - 135$ degrees with gantry	– future possibilities to avoid bending magnets by using optical mirrors
Gantry	– large size $(100 - 250$ tons) – diagnostic system cannot be set near patient	– small size $(1 - 10$ tons) – diagnostic system can be combined with gantry
Scanning	– mainly long pulse injection – recently started	– short pulses superimposed – main method
Energy	– up to 230 MeV (HIBMC)	– several tens of MeVs currently
Change of energy	– much time	– easy and rapid
Technology	– mature (started since 1930s)	– nascent (started since 1990s) – many elements to be developed
Cost	– expensive (23 billion yen (HIBMC))	– relatively inexpensive
Others		– protective goggle required
Clinical applications	– solid tumour in the body	– small sized tumours in the eye, thyroid, larynx, nasal or paranasal cavity, breast, superficial lymph node, skin, subcutaneous
Range	– 32 cm (whole body)	– several cm (superficial tumuor)

Table 4.1: Characteristics of a laser driven particle therapy machine and comparison between a conventional particle accelerator and a laser proton accelerator (at present); HIBMC is an acronym for Hyogo Ion Beam Medical Center in Japan; partial info taken from [19]

4.3 ELIMED and ELI Beamlines

4.3.1 ELI Beamlines

The aim of project Extreme Light Infrastructure (ELI) is to build a European net of research facilities with the latest laser equipment in the world. ELI will cover many research programs with need of high intensities, being 10 times higher than current achievable values. Moreover, the project will provide ultra-short laser pulses of a few tens femtoseconds duration and laser power up to 10 PW [2]. Because of these new techniques for medical image-display and diagnostics, radiotherapy, hadrontherapy, tools for new materials developing and testing, the latest in X-ray optics, etc. will be developed. In addition ELI will be a great education and work opportunity for scientists, engineers and students.
ELI will consist of three laser centers combined under one heading. These centers will be located in three European countries:

- The Czech Republic – *ELI Beamlines* is being built in Dolní Břežany as a facility for the generation of new secondary sources for interdisciplinary applications in physics, medicine, biology and the material sciences
- Hungary – *ELI Attosecond* will be a center for physics of ultra short optical pulses in attosecond order
- Romania – *ELI Nuclear Physics* will be focused on photonuclear physics

A place for another infrastructure is still under discussion. In addition to the funding countries, the major partners of the project preparatory phase, such as Germany, Great Britain, Italy and France, are also involved in the project.
The building of ELI Beamlines are designed by a British company Boggle Architects. An artistic view of the future ELI Beamlines building is shown in Fig. 4.6 and the location of experimental halls is shown in Fig. 4.7.

Figure 4.6: Aerial view of ELI Beamlines; [2]

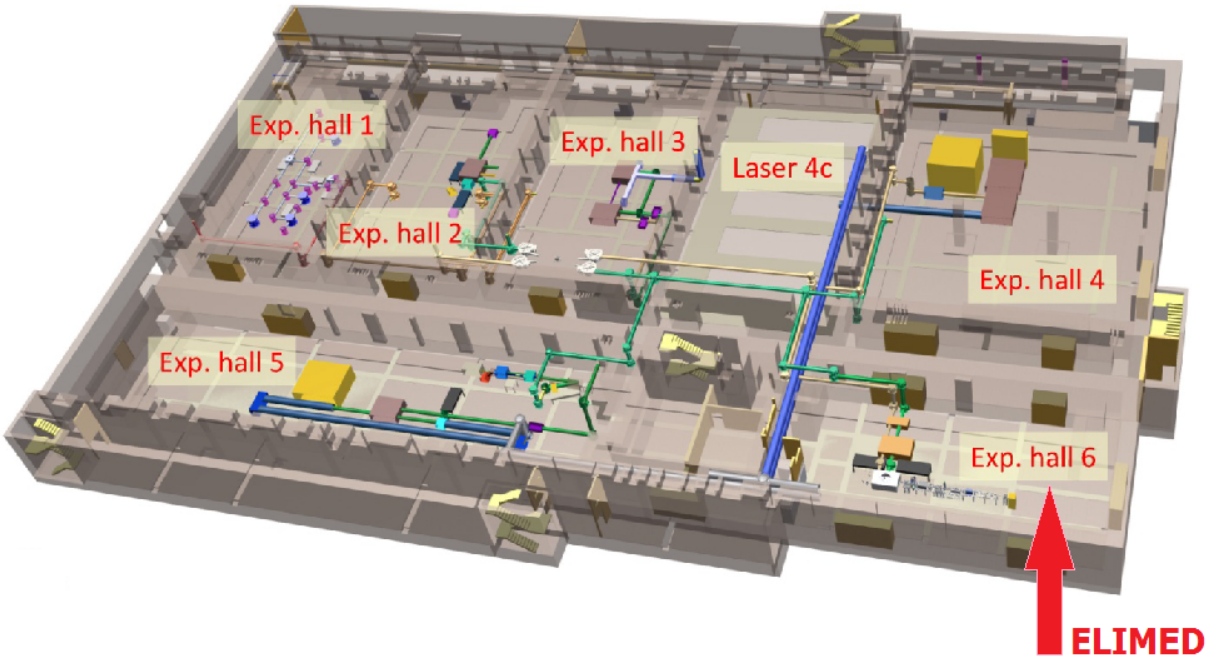

Figure 4.7: Plan of experimental halls in ELI Beamlines; [27]

4.3.2 ELIMED – a new hadron therapy concept based on laser-driven ion beams

ELIMED is one of the ELI's projects and its acronym means *ELI*-Beamlines *MED*ical and multidisciplinary applications.
The main areas of investigation which ELIMED will cover and general users' requirements are listed in Tab. 4.2 [27].

Investigation	Requirements
irradiation of biological and other samples	wide energy and fluency range; possibility of in-air irradiation
radiation damage on different components	homogeneous lateral beam distribution
demonstration of new irradiation modalities for radiotherapy	stability in terms of energy and fluency distributions
detector characterization	variable beam spot size (from 2 mm up to 40 mm); different ion species
pump probe investigation	beam control (diagnostics and dosimetry) with $< 5\%$ errors

Table 4.2: ELIMED's areas of investigation and user requirements; [27]

Laser driven ion beams, which will be generated at ELIMED, have great potential for demonstrating, improving and studying laser driven hadrontherapy, but will not be immediately suitable for medical applications. In fact, medical applications require better parameters in terms of beam characteristics and performance, especially those in delivery system, diag-

nostic tools or efficiency of beam transport, which will need time to be optimized.
A simplified layout of ELIMED beamline is shown in Fig. 4.8. Firstly, the ion beam is accelerated (discussed in chapter 1), then it enters the area for capturing and selection (theoretically discussed in chapter 2) which is the part I have been focusing on. Moreover, this is the part I was working on. As reported in chapter 3 I have written a program which can compute the particles trajectories in a solenoid magnetic field. Focusing and transport section, realized by the quadrupoles, follows and finally, the energy selection system ends the beamline.

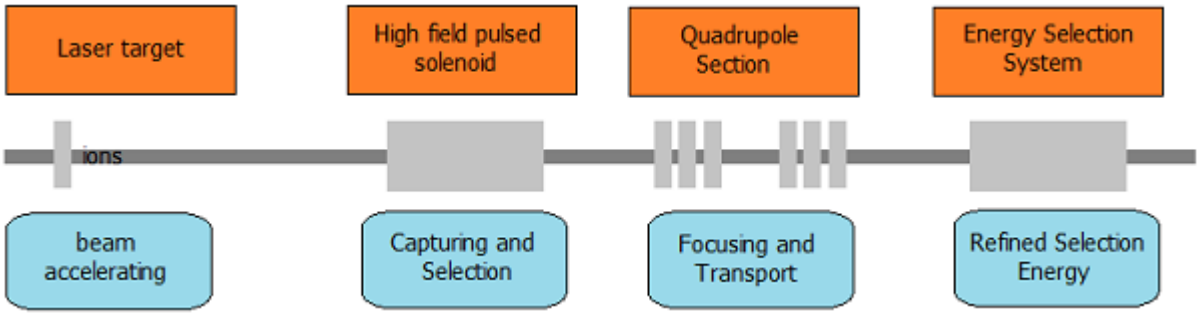

Figure 4.8: A simplified layout of ELIMED beamline

Two possible layouts for the beam transport section are shown in Fig. 4.9. Case A maximizes the transmission efficiency ($> 50\%$), but its disadvantage is the high energy spread ($> 50\%$). Case B maximizes the energy spread of the pre-section beams ($< 40\%$), but its disadvantage is the low transmission efficiency ($< 30\%$).

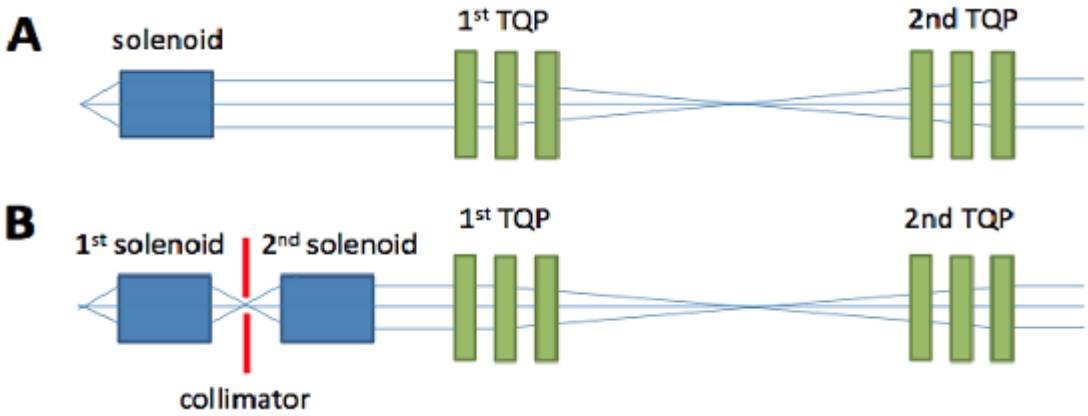

Figure 4.9: Possible layouts of collecting and transport section; cases A and B are discussed in text; [27]

The first challenge that lays ahead is to reach the following parameters: 60 MeV proton energy (eye tumour range), 10^{10} proton per laser pulse with 1 PW laser power and 30 fs duration of the laser pulse. In a graphic table in Fig. 4.10, the best and worst scenario for the first phase of the ELIMED beamline is reported.

Beam line solution: solenoid + quadrupoles + energy selector (8 m)

The worst case: 1 PW laser, 30J, 30 fs, 40° total divergency, TNSA regime, RR < 1Hz

Proton energy [MeV]	Energy spread [%]	Transmission efficiency [%]	Estimated incoming particles [ppb]	Estimated transmitted particles [ppb]	Estimated dose [Gy]
60,0	100	5,0	10^{10}	$5*10^{8}$	0,1

The best case: 1 PW laser, 30J, 30 fs, 5% energy spread, 5° divergency, DCE regime, RR < 1Hz

Proton energy [MeV]	Energy spread [%]	Transmission efficiency [%]	Estimated incoming particles [ppb]	Estimated transmitted particles [ppb]	Estimated dose [Gy] (*)
60,0	5	95,0	10^{12}	$9,5*10^{11}$	190 Gy (3 cm beam spot size)

Figure 4.10: The best and worst case of our expectation; [27]

Summary and Conclusions

The original part of this thesis work consists of developing a software for ion beam transport in magnetic solenoid fields aimed at decreasing the divergence of laser driven ion beams. A general description of the framework in which this work is developed is reported as well as the identification of the basic tools needed for the implementation of the software.
The aim of the first chapter is to describe basic concepts of the processes involved in laser driven ion beam acceleration (high intensity laser interaction with matter, absorption mechanisms, laser driven acceleration mechanisms). The second chapter deals with describing the classic behaviour of charged particle beams propagating in a solenoid magnetic field. The particle beam emittance is also defined and explained from a statistical point of view. The last chapter looks into laser-driven medical applications, both from a clinical and a physical point of view, and in particular to a future use of such non-conventional beams in hadrontherapy. Moreover the comparison to X-ray therapy, as well as the comparison between conventional and laser accelerators, is reported.
The software which has been developed is written in MATLAB. It can compute trajectory coordinates of a charged particle beam in a solenoid with given starting conditions for position and velocity coordinates. The software also takes the ion beam emittance into account. A possibility of investigating interesting effects of charged beams propagating in solenoid magnetic fields is demonstrated simply by changing few parameters, e.g. the fringing field effects. Moreover the software provides a plot of the particle trajectories giving a snapshot of the ion beam propagation.
The work can be potentially extended and completed in the upcoming future. In fact, different solutions for the optimization of the "capturing and selection" sector of the ELIMED beamline can be investigated. For instance, the geometry with two solenoids can be studied in order to minimize the energy spread of the "pre-selected" ion beams ($< 40\%$). However the disadvantage of this geometry is the low transmission efficiency ($< 30\%$). Therefore different geometries aimed at maximizing the transmission efficiency could be studied. Finally, after the optimization of the solenoid sector, the work could proceed with the design of a quadrupole system aimed at focusing the ion beam for a better transport. Moreover, numerical simulations will be needed for a better understanding of the physical picture.
Big challenges in research lay ahead of us, especially for medical applications of such beams, e.g. hadrontherapy. In fact, although several facilities based on conventional acceleration machines are operational worldwide, laser-driven hadrontherapy centers are still not present since they do not fit with the strict radiological requirements (energy, dose, etc.) yet. Beside technical aspects, the biological consequence of short ion bunches associated with ultrashort laser pulses have to be better investigated and understood. Furthermore, there are other potential applications of laser driven ion beams, e.g. triggering and control of nuclear reactions, production and probing of warm dense matter, and many others.

Bibliography

[1] William Barletta. USPAS notes about emittance for teaching purpose. 2012.

[2] ELI Beamlines. About project [online]. http://www.eli-beams.eu/about/, 2011. Accessed: 2013-05-26.

[3] Triumf Canada's national laboratory for particle and nuclear physics. Proton therapy [online]. http://www.triumf.ca/node/1641, 2009. Accessed: 2013-05-26.

[4] Nicolas Delerue. Emittance (and Liouville's theorem) [online]. http://www-pnp.physics.ox.ac.uk/~delerue/accelerator_option/6_emittance.pdf, 2006. Accessed: 2013-05-26.

[5] J. Fuchs, P. Antici, E. d'Humieres, E. Lefebvre, M. Borghesi, E. Brambrink, CA. Cecchetti, M. Kaluza, V. Malka, M. Manclossi, et al. Laser-driven proton scaling laws and new paths towards energy increase. *Nature Physics*, 2(1):48–54, 2005.

[6] Brian Hahn and Dan Valentine. *Essential MATLAB for engineers and scientists*. Newnes, 2007.

[7] Simon Jolly. Focusing Properties of a Solenoid magnet, UKNFIC meeting [online]. http://www.hep.ph.ic.ac.uk/uknfic/meetings/120505/SJ_Sol-focus_12-05-05.ppt, May 2005. Accessed: 2013-05-26.

[8] Vinit Kumar. Understanding the focusing of charged particle beams in a solenoid magnetic field. *American Journal of Physics*, 77:737, 2009.

[9] Julia Layton. Is proton therapy better than traditional radiation for cancer treatment? [online]. http://science.howstuffworks.com/life/human-biology/proton-therapy1.htm, 2007. Accessed: 2013-05-26.

[10] Arlene Lennox. Hadron therapy for cancer treatment, seminar in Fermilab [online]. http://www-bd.fnal.gov/ntf/reference/hadrontreat.pdf, 2003. Accessed: 2013-05-26.

[11] JC Lighthall, BB Back, SI Baker, SJ Freeman, HY Lee, BP Kay, ST Marley, KE Rehm, JE Rohrer, JP Schiffer, et al. Commissioning of the helios spectrometer. *Nuclear Instruments and Methods in Physics Research Section A: Accelerators, Spectrometers, Detectors and Associated Equipment*, 622(1):97–106, 2010.

[12] Pasquale Londrillo, Graziano Servizi, Andrea Sgattoni, Stefano Sinigardi, Marco Sumini, and Giorgio Turchetti. Protons Acceleration by CO2 Laser Pulses and Perspectives for Medical Applications.

[13] Andrea Macchi. High Intensity Laser-Solid Interaction: Collisionless Absorption and Instabilities [online]. `www.df.unipi.it/~macchi`, 2004. Accessed: 2013-05-26.

[14] Andrea Macchi, Marco Borghesi, and Matteo Passoni. Ion acceleration by superintense laser-plasma interaction. *arXiv preprint arXiv:1302.1775*, 2013.

[15] M. Mahdavi and SF. Ghazizadeh. Linear Absorption Mechanisms in Laser Plasma Interactions. *Journal of Applied Sciences*, 12:12–21, 2012.

[16] D Margarone, O Klimo, IJ Kim, J Prokupek, Jiri Limpouch, TM Jeong, T Mocek, J Psikal, HT Kim, J Proska, et al. Enhanced TNSA acceleration with 0.1-1 PW lasers. In *SPIE Optics+ Optoelectronics*, pages 878023–878023. International Society for Optics and Photonics, 2013.

[17] K. Markey. Laser-ion acceleration – towards table top accelerators.

[18] Peter Mulser and Dieter Bauer. *High power laser-matter interaction*, volume 238. Springer, 2010.

[19] Masao Murakami, Yoshio Hishikawa, Satoshi Miyajima, Yoshiko Okazaki, Kenneth L. Sutherland, Mitsuyuki Abe, Sergei V. Bulanov, Hiroyuki Daido, Timur Zh Esirkepov, James Koga, et al. Radiotherapy using a laser proton accelerator. *arXiv preprint arXiv:0804.3826*, 2008.

[20] Rod Nave. Cyclotron [online]. `http://hyperphysics.phy-astr.gsu.edu/hbase/magnetic/cyclot.html`, 2013. Accessed: 2013-05-26.

[21] Harald Paganetti and Thomas Bortfeld. Proton Beam Radiotherapy - The state of the art. *in: New Technologies in Radiation Oncology (Medical Radiology Series),(Eds.) W. Schlegel, T. Bortfeld and A.-L. Grosu, Springer Verlag, Heidelberg, ISBN*, pages 3–540, 2005.

[22] Matteo Passoni, Luca Bertagna, and Alessandro Zani. Target Normal Sheath Acceleration at ultrahigh intensities: a theoretical parametric investigation. *The 2nd international confernce on ultra-intense laser interaction science, Rome, Italy*, 4, 2009.

[23] Matteo Passoni, Luca Bertagna, and Alessandro Zani. Target normal sheath acceleration: theory, comparison with experiments and future perspectives. *New Journal of Physics*, 12(4):045012, 2010.

[24] ProCure. The Healing Power of Protons [online]. `http://www.procure.com/ProtonTherapy.aspx`, 2012. Accessed: 2013-05-26.

[25] Michael Richmond. Solenoids and Magnetic Fields [online]. `http://spiff.rit.edu/classes/phys313/lectures/sol/sol_f01_long.html`, 2007. Accessed: 2013-05-26.

[26] Marius Schollmeier. Proton energy scaling laws - Generation of above-100-MeV proton beams with Z-Petawatt? [online]. `http://www.ph.utexas.edu/~iheds/2009talks/Schollmeier_IHEDS2009.pdf`, 2009. Accessed: 2013-05-26.

[27] Valentina Scuderi. ELIMED: a new hadron therapy concept based on laser-driven ion beams, 2013.

[28] South Australian Medical Heritage Society Inc. Radiotherapy and Bragg's Peak [online]. http://samhs.org.au/Virtual%20Museum/xrays/Braggs-peak-rxth/braggpeakrxth.htm, May 2013. Accessed: 2013-06-15.

[29] Derek A. Tidman and Nicholas A. Krall. Shock waves in collisionless plasmas. *Wiley Series in Plasma Physics, New York: Wiley-Interscience, 1971*, 1971.

[30] Helmut Wiedemann. *Particle accelerator physics*. Springer, 2007.

[31] Wikipedia. Ampere's circuital Law [online]. http://en.wikipedia.org/wiki/Amp%C3%A8re's_circuital_law, May 2013. Accessed: 2013-05-26.

[32] Wikipedia. Beam emittance [online]. http://en.wikipedia.org/wiki/Beam_emittance, 2013. Accessed: 2013-05-26.

[33] Wikipedia. Biot-Savart Law [online]. http://en.wikipedia.org/wiki/Biot_savart, May 2013. Accessed: 2013-05-26.

[34] Wikipedia. Debye length [online]. http://en.wikipedia.org/wiki/Debye_length, May 2013. Accessed: 2013-05-26.

[35] Wikipedia. Del in cylindrical and spherical coordinates [online]. http://en.wikipedia.org/wiki/Del_in_cylindrical_and_spherical_coordinates, 2013. Accessed: 2013-05-26.

[36] Wikipedia. Gray (unit) [online]. http://en.wikipedia.org/wiki/Gray_(unit), May 2013. Accessed: 2013-05-26.

[37] Wikipedia. Larmorova rotace. http://cs.wikipedia.org/wiki/Larmorova_rotace, 2013. Accessed: 2013-05-26.

[38] Wikipedia. Radiation presure [online]. http://en.wikipedia.org/wiki/Radiation_pressure, 2013. Accessed: 2013-05-26.

[39] Wikipedia. Root mean square (RMS) [online]. https://en.wikipedia.org/wiki/Root_mean_square, May 2013. Accessed: 2013-05-26.

[40] Wikipedia. Synchrotron [online]. http://en.wikipedia.org/wiki/Synchrotron, 2013. Accessed: 2013-05-26.

[41] Wikipedia. Taylorova řada (taylor series) [online]. http://cs.wikipedia.org/wiki/Taylorova_%C5%99ada, 2013. Accessed: 2013-05-26.

[42] Wikipedia. Vlasov equation [online]. http://en.wikipedia.org/wiki/Vlasov_equation#The_Vlasov.E2.80.93Maxwell_system_of_equations_.28cgs_units.29, May 2013. Accessed: 2013-05-26.

[43] Wikipedia. WKB approximation [online]. http://en.wikipedia.org/wiki/WKB_approximation, 2013. Accessed: 2013-05-26.

[44] T. Mendez Y. Liu and P. E. Mueller. Hands-on Notes: Beam Emittance Characterization [online]. http://fribusers.org/4_GATHERINGS/2_SCHOOLS/2010/hands_on/handout_3a.pdf, 2010. Accessed: 2013-05-26.

Appendix

Institution	Where	First Tr.	Last Tr.	# of patients	Date of Total
Berkeley 184	CA, USA	1954	1957	30	
Uppsala	Sweden	1957	1976	73	
Harvard	MA, USA	1961	2002	9116	
Dubna	Russia	1967	1996	124	
ITEP, Moscow	Russia	1969		3748	June-04
St. Petersburg	Russia	1975		1145	April-04
Chiba	Japan	1979		145	April-02
PMRC, Tsukuba	Japan	1983	2000	700	
PSI (72 MeV)	Switzerland	1984		4066	June-04
Dubna	Russia	1999		191	Nov-03
Uppsala	Sweden	1989		418	Jan-04
Clatterbridge	England	1989		1287	Dec-03
Loma Linda	CA, USA	1990		9282	July-04
Louvain-la-Neuve	Belgium	1991	1993	21	
Nice	France	1991		2555	April-04
Orsay	France	1991		2805	Dec-03
iThemba LABS	South Africa	1993		446	Dec-03
MPRI	IN, USA	1993	1999	34	
UCSF - CNL	CA, USA	1994		632	June-04
TRIUMF	Canada	1995		89	Dec-03
PSI (200 MeV)	Switzerland	1996		166	Dec-03
H. M. I, Berlin	Germany	1998		437	Dec-03
NCC, Kashiwa	Japan	1998		270	June-04
HIBMC, Hyogo	Japan	2001		359	June-04
PMRC, Tsukuba	Japan	2001		492	July-04
NPTC, MGH	MA, USA	2001		800	July-04
INFN-LNS,Catania	Italy	2002		77	June-04
WERC	Japan	2002		14	Dec-03
Shizuoka	Japan	2003		69	July-04
MPRI	IN, USA	2004		21	July-04

Table 4.3: World wide proton therapy experience as of July 2004; [21]

```
%%%%%%%%%%%%%%%%%%%%%%%%%%%%%%%%%%%%%%%%%%%%%%%%%%%%%%%%%%%%%%%%%%%%%%%
%%%%%%%%%%%%%%%%%%%%%%%%   MAIN CODE   %%%%%%%%%%%%%%%%%%%%%%%%%%%%%%%%
%%%%%%%%%%%%%%%%%%%%%%%%%%%%%%%%%%%%%%%%%%%%%%%%%%%%%%%%%%%%%%%%%%%%%%%
clf
time=cputime;
%
% set solenoid parameters
%
i = 1800;              % wire current [A]
N = 1200;              % number of wire turns
zini = 0.1;            % z position of the left end of the solenoid [m]
zfin = 0.25;           % z position of the right end of the solenoid [m]
r  = 0.025;            % solenoid radius [m]
bo=(1.26E-6*i*N)/sqrt((zfin-zini)^2+4*r^2) % mag. field in the sol. centre
%
% set beam parameters
%
energy= 30e6;             % kinetic energy [eV]
Eo=938e6;                 % proton rest energy [eV]
gamma=1+energy/Eo;        % gamma relativistic factor
beta=sqrt(1-1/gamma^2);  % beta velocity
velmod=beta*(2.998e+8);  % total velocity
%
% ODE time set
%
Ltot=1;         % maximum length of total path, from this calculation we
                % can get the total time tmax for the particle motion
tmin0=0;
tmax0=Ltot/velmod; % [s]
tspan0=[tmin0:tmax0/1000:tmax0];
%
% convert Cartesian coordinates (generated from the beam_emittance
% function) to cylindrical ones
%
[ttheta,rr,zz]=cart2pol(posx(:,1)/1000,posx(:,2)/1000,0); %transformation
% from Cartesian to cylindrical coordinates (ttheta,rr,zz)
r0=[rr,ttheta];
velr=sqrt((posxp(:,1)*velmod/1000).^2+(posxp(:,2)*velmod/1000).^2);
% realistic approach also possible:
%[ttheta,rr,zz]=cart2pol(posx(:,1)/10000,posx(:,2)/10000,0);
%r0=[rr,ttheta];
%velr=sqrt((posxp(:,1)*velmod/100).^2+(posxp(:,2)*velmod/100).^2);
k=1;
%
% differential equations (solving)
%
for row=1:1:Np;     % for Np particles with 1-particle step
y0=[r0(row,1),velr(row),r0(row,2),0,0,sqrt(velmod^2-velr(row)^2)];
% velmod is total velocity, v_theta is 0
options=odeset('reltol',1e-7);
[t0,y]=ode45('solutionODEcylind3D',tspan0,y0,options,i,N,zini,zfin,r);
cylcoord(:,:,k)=y;  % saving information form ODEs for each k-th particle
```

```
k=k+1;

end
%
%  convert cylindrical coordinates to Cartesian ones because of plotting
%
for kk=1:1:(k-1)
[xx,yy,zz]=pol2cart(cylcoord(:,3,kk),cylcoord(:,1,kk),cylcoord(:,5,kk));
end
for kk=1:1:(k-1)
[xx(:,kk),yy(:,kk),zz(:,kk)]=pol2cart(cylcoord(:,3,kk),cylcoord(:,1,kk),
cylcoord(:,5,kk));
end
for kk=1:1:(k-1)
coord(:,:,kk)=[xx(:,kk),yy(:,kk),zz(:,kk)]; % saving in coord
end
%
%  plot trajectories
%
for k=1:1:Np % for each of Np particles
    hold on
    subplot(2,2,1);
    plot(coord(:,3,k),coord(:,2,k)); %zy plane
    hold off
    hold on
    subplot(2,2,2);
    plot(coord(:,3,k),coord(:,1,k)); %zx plane
    hold off
    hold on
    subplot(2,2,3);
    plot(coord(:,2,k),coord(:,1,k)); %yx plane
    hold off
    hold on
    subplot(2,2,4);
    plot3(coord(:,3,k),coord(:,2,k),coord(:,1,k)); %simple 3D
    hold off

end

e=cputime-time
```

Published with MATLAB® 7.13

```
%%%%%%%%%%%%%%%%%%%%%%%%%%%%%%%%%%%%%%%%%%%%%%%%%%%%%%%%%%%%%%%%%%%%%%%
%%%%%%%%%%%%%%   SOLUTION OF CYLINDRICAL ODEs   %%%%%%%%%%%%%%
%%%%%%%%%%%%%%%%%%%%%%%%%%%%%%%%%%%%%%%%%%%%%%%%%%%%%%%%%%%%%%%%%%%%%%%
function [dydt]=f(t,y,nothing,i,N,zini,zfin,r)
amu=1.66053886e-27;             % atomic mass unit [kg]
charge = 1.60217653e-19;        % elementary charge [C]
Ap=1.00727647;                  % mass number proton (= mass of proton
                                % divided by 1u (atomic mass unit)
Q = 1;                          % charge state
mu_0=1.26E-6;                   % permeability constant [H/m]
L = (zfin - zini);              % length of solenoid [m]
z2 = y(5) - zini;
z1 = y(5) - zfin;
bz=(mu_0*i*N)/(2*L)*(z2/sqrt(z2*z2+r*r)-z1/sqrt(z1*z1+r*r)); %[T]
btheta=0;
br=-0.5*y(1)*(mu_0*i*N)/(2*L)*(1/sqrt(z2*z2+r*r)-1/sqrt(z1*z1+r*r)-
        -z2*z2/(z2*z2+r*r)^(1.5)+z1*z1/(z1*z1+r*r)^(1.5));
ratio_QA=Q/Ap*charge/amu;
   dydt=[y(2)
        ratio_QA*y(1)*y(4)*bz+y(1)*y(4)^2                % focusing
      y(4)
        (ratio_QA*(y(6)*br-y(2)*bz)-2*y(2)*y(4))/y(1)      % rotation
      y(6)
        -ratio_QA*y(1)*y(4)*br];                         % acceleration
```

Published with MATLAB® 7.13

```
%%%%%%%%%%%%%%%%%%%%%%%%%%%%%%%%%%%%%%%%%%%%%%%%%%%%%%%%%%%%%%%%%%%%%%%
%%%%%%%%%%%%%%%%%%%%%%  BEAM EMITTANCE  %%%%%%%%%%%%%%%%%%%%%%%%%%%%%%%%
%%%%%%%%%%%%%%%%%%%%%%%%%%%%%%%%%%%%%%%%%%%%%%%%%%%%%%%%%%%%%%%%%%%%%%%
clear all;
time=cputime;
% twiss parameters
gamma=15
alpha=-2   % beta*gamma-alpha^2=1
beta=(1+alpha^2)/gamma
%
eps0=5;                    % RMS emittance [pi*mm*mrad]
Np=100;                    % particles number
xrms=sqrt(eps0*beta)       % [mm]
xprms=sqrt(eps0*gamma)     % [mrad]
count=0;                   % a counter
posx=zeros(Np,2);          % allocate memory array for x and y plane;
                           % Np-by-2 array of zeros
                           % a storage for coordinates
posxp=zeros(Np,2);         % allocate memory array for x' and y' plane
                           % a storage for divergences
emittance=zeros(Np,2);     % allocate memory array
while count<Np
    x=normrnd(0,xrms,1,2);   % Gaussian distribution with sigma=xrms(x,y),
                             % mu=0; generates an 1-by-2-by random array
    xp=normrnd(0,xprms,1,2); % Gaussian distribution with sigma=xprms(x',y')
    eps= gamma*x.^2+2*alpha*x.*xp+beta*xp.^2; % calculate the emittance
                                              % considering twiss par.

    if eps<9*eps0 & sqrt(x(1,1)^2+x(1,2)^2)<3*xrms;
        count=count+1;
        posx(count,:)=x; % here coordinates are stored,
                         % posx(count,1) and posx(count,2)
        posxp(count,:)=xp; % here divergences are stored
        emittance(count,:)=eps;
    end % from this we have x, x', y, y', x=(x,y), xp=(x',y') and emittance
end
plot(posx(:,1),posxp(:,1),'.'); axis equal; %x-x' plane
e_time=cputime-time
```

Published with MATLAB® 7.13

```
%%%%%%%%%%%%%%%%%%%%%%%%%%%%%%%%%%%%%%%%%%%%%%%%%%%%%%%%%%%%%%%%%%%%%%%
%%%%%%%%%%%%%%%%%%    ENERGY CALCULATION    %%%%%%%%%%%%%%%%%%%%%%%%
%%%%%%%%%%%%%%%%%%%%%%%%%%%%%%%%%%%%%%%%%%%%%%%%%%%%%%%%%%%%%%%%%%%%%%%
clear velocity;
kkk=1
for kk=1:1:Np
velocity(:,:,kk)=sqrt(coord(kkk,2,kk)^2+coord(kkk,4,kk)^2+coord(kkk,6,kk)^2);
% velocity for each particle
kkk=kkk+1;
end
beta1=velocity/(2.998e+8); % relativistic factors beta, gamma
gamma1=1/sqrt(1-beta1.^2);
Ekin1=(gamma1-1)*Eo;
```

Published with MATLAB® 7.13

```
%%%%%%%%%%%%%%%%%%%%%%%%%%%%%%%%%%%%%%%%%%%%%%%%%%%%%%%%%%%%%%%%%%%%%%%
%%%%%%%%%%%%%%%%%%   PLOTTING EMITTANCES   %%%%%%%%%%%%%%%%%%%%
%%%%%%%%%%%%%%%%%%%%%%%%%%%%%%%%%%%%%%%%%%%%%%%%%%%%%%%%%%%%%%%%%%%%%%%
subplot(2,1,1);
plot(posx(:,1),posxp(:,1),'.');  %emittance x-x';
axis square;
subplot(2,1,2);
plot(posx(:,2),posxp(:,2),'.');  %emittance y-y'
axis square;
```

Published with MATLAB® 7.13